

AD-A090 332

SINGER CO LITTLE FALLS NJ KEARFOTT DIV

F/6 20/10

RELAXATION PHENOMENA IN OPTICALLY PUMPED MERCURY ISOTOPES.(U)

AUG 80 P A HEIMANN, J H SIMPSON, M J KELLY

F49620-76-C-0009

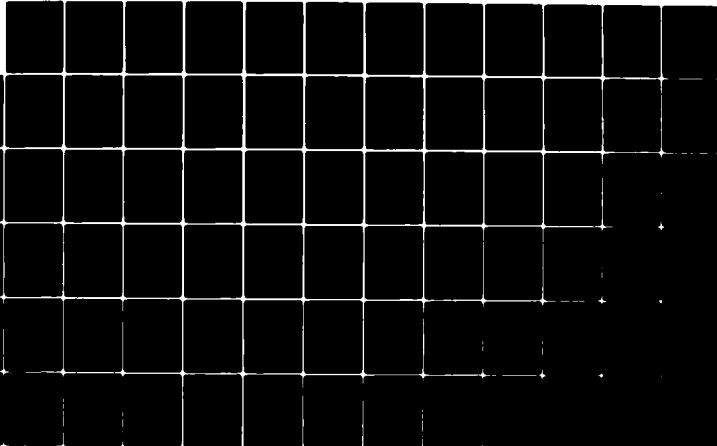
UNCLASSIFIED

KO-80-22

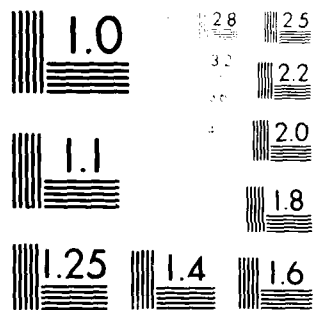
AFOSR-TR-80-0744

NL

1 OF 1
AD-A090 332



END



MINIMUM RESOLUTION TEST CHART
 NATIONAL BUREAU OF STANDARDS-1963-A

UNCLASSIFIED

SECURITY CLASSIFICATION OF THIS PAGE (When Data Entered)

REPORT DOCUMENTATION PAGE		READ INSTRUCTIONS BEFORE COMPLETING FORM
1. REPORT NUMBER AFOSR-TR-80-0744	2. GOVT ACCESSION NO. AD-A090332	3. RECIPIENT'S CATALOG NUMBER
4. TITLE (and Subtitle) Relaxation Phenomena in Optically Pumped Mercury Isotopes		5. TYPE OF REPORT & PERIOD COVERED Interim Scientific Report 1 Jul 1979-30 June 1980
7. AUTHOR(s) R.A. Heimann, J.H. Simpson, and M.J. Kelly		6. PERFORMING ORG. REPORT NUMBER KD-80-22
9. PERFORMING ORGANIZATION NAME AND ADDRESS The Singer Co., Kearfott Div. 1225 McBride Avenue Little Falls, N.J. 07424		8. CONTRACT OR GRANT NUMBER(s) F49260-76-C-0009
11. CONTROLLING OFFICE NAME AND ADDRESS Air Force Office of Scientific Research Building 410, Bolling AFB /N/P Washington, D.C. 20332		10. PROGRAM ELEMENT, PROJECT, TASK AREA & WORK UNIT NUMBERS 2301/A4 01102F
14. MONITORING AGENCY NAME & ADDRESS (if different from Controlling Office) LEVEL		12. REPORT DATE August 15, 1980
		13. NUMBER OF PAGES 80
		15. SECURITY CLASS. (of this report) Unclassified
16. DISTRIBUTION STATEMENT (of the Report) Approved for public release; distribution unlimited.		15a. DECLASSIFICATION/DOWNGRADING SCHEDULE
17. DISTRIBUTION STATEMENT (of the abstract entered in Block 20, if different from Report) DTIC OCT 6 1980		
18. SUPPLEMENTARY NOTES		
19. KEY WORDS (Continue on reverse side if necessary and identify by block number) Magnetic Relaxation, Optical Pumping, Nuclear Magnetic Resonance, Mercury Isotopes, Quadrupole Moment, Perturbation, Mercury (Metal), Metal Vapors, Silicon Dioxide, Surface Properties, Ultraviolet Radiation, Nuclear Spin, Gyroscopes.		
20. ABSTRACT (Continue on reverse side if necessary and identify by block number) The origins and effects of both randomly-fluctuating and steady- state quadrupole perturbations on ^{201}Hg have been clarified greatly. These perturbations are an unavoidable consequence of the adsorp- tion of ^{201}Hg on the cell wall, and are not greatly affected by the fine details of the surface at the adsorption site. A complete description of a quadrupole perturbation must include effects such as torques on the nucleus, in addition to including the shift in		

DD FORM 1 JAN 73 1473

EDITION OF 1 NOV 65 IS OBSOLETE

UNCLASSIFIED

SECURITY CLASSIFICATION OF THIS PAGE (When Data Entered)

80 9 25 072

DDC FILE COPY

UNCLASSIFIED

SECURITY CLASSIFICATION OF THIS PAGE(When Data Entered)

the Zeeman energy levels. A calculation using such a complete description predicted that the relaxation rate of ^{201}Hg in a cube-shaped cell should be independent of cell orientation. This prediction was verified experimentally. Another calculation, which modelled ^{201}Hg as a single four-level spin system instead of three two-level spin systems, predicted a functional form for the non-exponential decay of ^{201}Hg in the presence of a quadrupole perturbation. These predictions were also verified experimentally.

Surface analysis of NMR cell walls detected only silicon and oxygen, and revealed no significant differences among surfaces of cells before heat treatment, after heat treatment, and after exposure to strong uv resonance radiation.

Experiments have revealed that the cell tip area is not the dominant relaxation site in cells prior to their first heat treatment, and that silica glassblower's smoke does not cause strong relaxation of mercury isotopes.

Accession No.	
NTIS	
DTIC	
Unannounced	
Justification	
By	
Director	
A	
Date	
A	

UNCLASSIFIED

SECURITY CLASSIFICATION OF THIS PAGE(When Data Entered)

AFOSR-TR- 80 - 0744

1. INTRODUCTION

	<u>PAGE</u>
1. INTRODUCTION	1
1.1 HIGHLIGHTS OF THE RESEARCH EFFORT	1
1.2 SUMMARY OF EXPERIMENTAL TECHNIQUES	4
2. EFFECTS DUE TO QUADRUPOLE PERTURBATIONS	8
2.1 INTRODUCTION	8
2.2 SOURCES OF QUADRUPOLE PERTURBATIONS	9
2.2.1 Perturbations Due to the Cell Wall	11
2.2.2 Perturbations Due to Light	13
2.2.3 Consistency of the Algebraic Signs of the Perturbations	14
2.3 DENSITY MATRIX AND SPHERICAL BASIS OPERATORS	15
2.4 NON-EXPONENTIAL DECAY	19
2.4.1 Theory	20
2.4.2 Experimental	25
2.5 COMBINED QUADRUPOLE PERTURBATION/TRANSVERSE MAGNETIC FIELD/PUMPING RADIATION/RELAXATION	28
2.6 RELAXATION DUE TO A FLUCTUATING ANISOTROPIC PERTURBATION	33
2.6.2 Example: Electric Field Gradient	40
2.6.3 Wall Relaxation for Various Container Shapes	42
2.6.4 Experimental	47
2.7 CONCLUSIONS	52
3. CELL FABRICATION AND TESTING	53
3.1 TIP-ONLY HEAT TREATMENTS	53
3.2 EFFECTS OF ABBREVIATED HEAT TREATMENT PROCEDURE	55
3.3 THE CAGNAC CELL STABILIZATION METHOD	56
3.4 WATER-FREE SPECTROSIL CELLS	58
3.5 MERCURY PURIFICATION	60
4. COMPLEMENTARY INVESTIGATIONS	62
4.1 SURFACE ANALYSIS OF CELL WALL MATERIALS	62
4.2 SILICA GLASSBLOWER'S SMOKE	63

THE SINGER COMPANY • KEARFOTT DIVISION

	<u>PAGE</u>
4.3 CORRELATION TIME OF THE WALL POTENTIAL DUE TO MOTION OF THE MERCURY ATOM	64
4.4 AVERAGE TRAVEL DISTANCE OF A MERCURY ATOM WITHIN A CELL	68
4.5 THE DARK FILM IN MERCURY LAMPS	68
5. PUBLICATIONS	71
5.1 THE DARK FILM IN MERCURY LAMPS	71
5.2 EFFECTS DUE TO QUADRUPOLE PERTURBATIONS	71
5.3 USE OF NMR RELAXATION AS A SURFACE ANALYSIS TECHNIQUE	71
6. SUGGESTIONS FOR FURTHER STUDY	73
7. REFERENCES	75
APPENDIX: RESEARCH OBJECTIVES & PERSONNEL	77

AIR FORCE OFFICE OF SCIENTIFIC RESEARCH (AFSC)
NOTICE OF TRANSMITTAL TO DDC
This technical report has been reviewed and is
approved for public release IAW AFR 190-12 (7b).
Distribution is unlimited.
A. D. BLOSE
Technical Information Officer

1. INTRODUCTION

This program is concerned with the physical phenomenon of the nuclear magnetic resonance relaxation of two isotopes, ^{199}Hg and ^{201}Hg , of vapor-phase mercury in contact with the walls of a container. The technique of orientation by optical pumping is employed to enhance the net nuclear magnetic moment, and optical techniques are also employed to monitor the dynamics of the nuclear spin system.

During part of the current reporting period, detailed calculations were carried out on the effects of steady-state and randomly-fluctuating quadrupole perturbations upon the dynamics of the ^{201}Hg spin system. These calculations are described in Chapter 2. The investigation of various cell fabrication and heat treatment techniques were continued, and is described in Chapter 3. Other experiments and calculations relevant to this project are presented in Chapter 4. Publications which resulted from these efforts are listed in Chapter 5, and suggestions for future studies are presented in Chapter 6. The remainder of this introductory chapter describes the important results obtained during this reporting period, and briefly describes the experimental method used for establishing and monitoring the nuclear spin distribution.

1.1 HIGHLIGHTS OF THE RESEARCH EFFORT

The work done during the reporting period has resulted in an improved understanding of the mechanisms responsible for the relaxation of the nuclear spins, has clarified the conditions which exist in the actual NMR cell, and has eliminated from consideration some of the mechanisms which had previously been suggested as causes for relaxation.

The origins and effects of both randomly-fluctuating and steady-state quadrupole perturbations on ^{201}Hg have been clarified greatly. It is now

understood that the randomly-fluctuating quadrupole perturbation, which is responsible for the relaxation of ^{201}Hg , is more a consequence of the adsorption of that atom than a consequence of the fine details of the surface at the adsorption site, since an electric field gradient, directed perpendicular to a surface, is a necessary condition for adsorption to occur. The correlation time of this randomly-fluctuating perturbation is approximately equal to the adsorbed atom's sticking time, which is determined by the strength of the adsorption. The relaxation time of ^{201}Hg is inversely proportional to both the strength and the correlation time of the fluctuating perturbation. Therefore, any mechanism which weakens the adsorption of mercury will cause both a weaker electric field gradient at the surface and a shorter sticking time, and will therefore increase the relaxation time of ^{201}Hg .

The expression for a quadrupole perturbation contains three terms, defined in Section 2.1. An energy-shift term describes the change in the magnetic energy levels, a torque term describes the torque felt by the nucleus, and a 2ω term is related to the coupling between levels whose quantum numbers m differ by two. In the past, only the energy-shift term has been considered, but the importance of the torque and 2ω terms in the quadrupole perturbation is now more fully appreciated. For instance, at $\theta = 55^\circ$, the energy-shift term of the quadrupole perturbation is zero, but the torque and 2ω terms are non-zero. This means that the nuclear spin feels a torque and can be relaxed, even though its magnetic energy levels have not been shifted by the perturbation. When the torque and 2ω terms are included in the description of a randomly-fluctuating quadrupole perturbation, the relaxation rate in a cube-shaped cell is found to be independent of cell orientation. This prediction has been verified by a careful experiment.

The effects of the energy-shift term of a steady-state quadrupole perturbation upon the dynamics of a ^{201}Hg spin system have been calculated in detail. Previous calculations had modelled the four-level ^{201}Hg spin

system as three separate two-level systems. Although such a model is simpler to use, it does not yield insights into the interrelationship of the various types of spin distributions (e.g., orientation and alignment distributions, both transverse and longitudinal to the external magnetic field) of this multi-level system. During the current reporting period, calculations were performed using spherical basis operators to describe the spin system. These calculations yielded a detailed functional form for the time dependence of signals from freely-precessing ^{201}Hg in the presence of a quadrupole perturbation. Several of these predictions were verified experimentally. In addition, the calculations yielded insights into the effects of a quadrupole perturbation combined with a transverse rf magnetic field. The steady-state distribution in this case is a linear combination of both orientation and alignment distributions, even if only one type of distribution is being replenished by optical pumping.

The variation of the phase difference between the precessing orientation distribution and the external rf field, as a function of parameters such as relaxation times, pumping rates, resonant frequency, and the frequency of the external rf field, has been examined. These results have yielded insights into the effects of the cell wall upon the steady-state dynamics of the spin system. These insights are expected to prove useful in the development of devices which make use of optically-pumped mercury vapor.

The elemental composition of the silica cell wall surface was investigated, using X-ray photoelectron spectroscopy. The mercury nuclei are believed to interact predominantly with the first few atomic layers of the interior cell wall. According to this analysis the wall surface is pure SiO_2 , with no mercury or other impurities present to within a 1% detection limit. The analysis did not reveal any significant difference in elemental composition among the surfaces of cells before heat treatment, after heat treatment, and after exposure to strong uv radiation.

The results of experiments performed during the reporting period have eliminated several previously-considered hypotheses for causes of mercury relaxation. Experimental results indicate that the surface near the cell tip area is not the dominant mercury relaxation site in cells prior to their first heat treatment, but that relaxation occurs to some degree over the entire cell surface. Silica glassblower's smoke consists of small particles of silicon dioxide, not monoxide, and it does not form a strong relaxing site, since a cell which contained visible amount of such smoke was found to have relaxation times comparable to other cells from the same batch which did not contain such smoke. Also, as stated above, the relaxation of ^{201}Hg due to electric field gradients does not vanish at certain orientations of the field, since the torque and 2ω terms must still be considered.

1.2 SUMMARY OF EXPERIMENTAL TECHNIQUES

The experimental method for monitoring the nuclear spin distribution has been described previously (see, for example, reference 1), and is summarized here.

The NMR signals are observed from mercury vapor in a container which is usually made from fused silica. Except for the cube-shaped cell described in Section 2.6.4, the cells are 1 cm diameter spheres. They are baked out under vacuum during fabrication, no buffer gas is intentionally introduced, and the mercury density is chosen to be sufficiently low so that the mercury interacts strongly only with the walls of the cell.

The experimental apparatus is shown in Figure 1.1. The 253.7 nm light from the ^{202}Hg readout lamp is slightly off resonance from hyperfine components of ^{199}Hg and ^{201}Hg absorptions,⁽²⁾ and it can be shown⁽³⁾ that if such light is directed perpendicular to the H_0 magnetic field and is elliptically polarized, then the direction of the axis of elliptical polarization is rotated through an angle proportional to the transverse

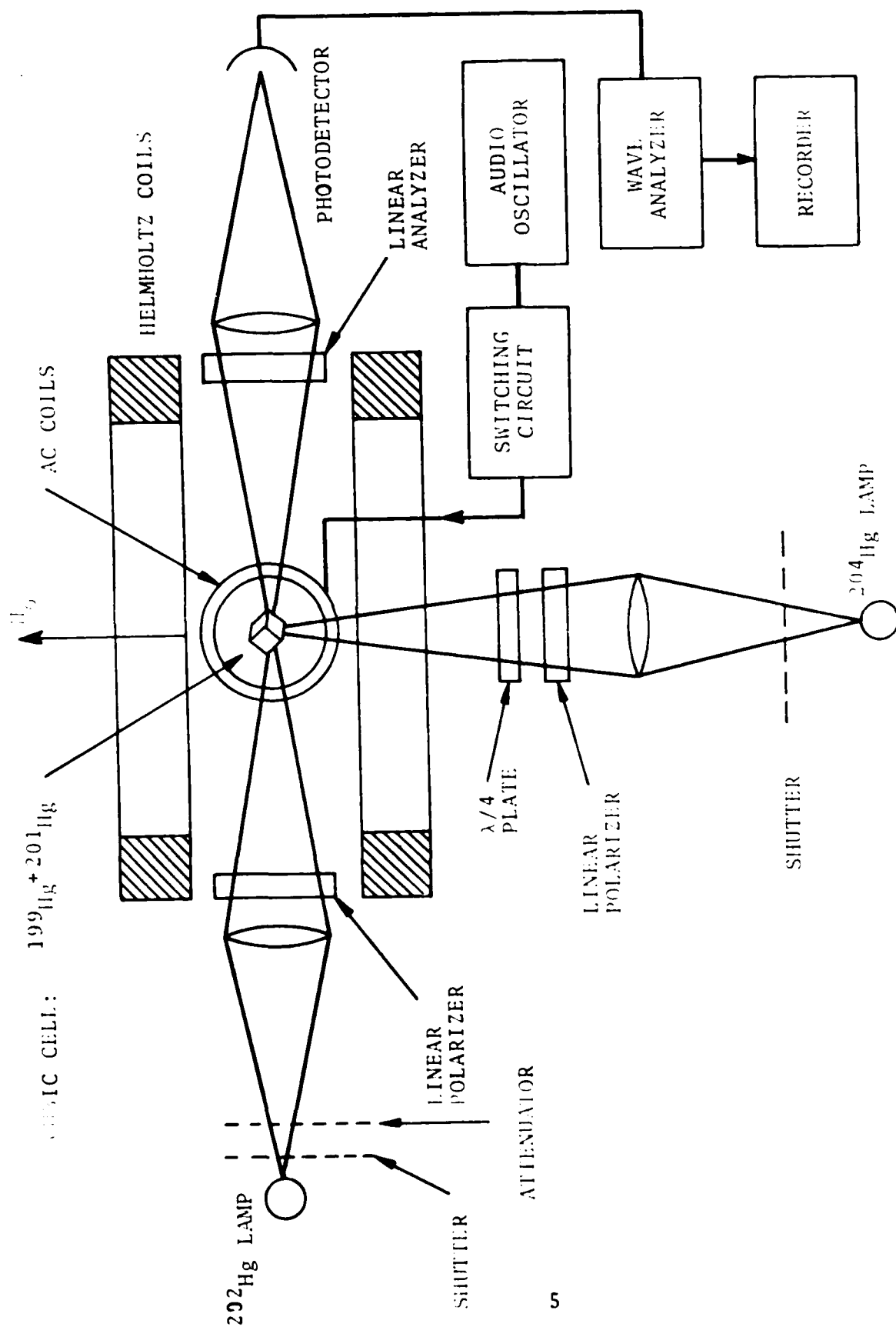


FIGURE 1.1.1 - Experimental Arrangement

orientation moment and the ellipticity of the polarization is changed by an amount proportional to the transverse alignment moment (these moments are defined in Section 2.3). The linear analyzer in front of the photodetector causes only the rotation of the polarization axis to be detected, causing a change in intensity at the photodetector. A quarter-wave plate placed in front of the analyzer would cause only the change in ellipticity to be detected. Therefore, it is possible to monitor either the orientation distribution or the alignment distribution individually.

A longitudinal spin distribution is created by optical pumping with a ^{204}Hg lamp, whose 253.7 nm light is absorbed efficiently by hyperfine components of both ^{199}Hg and ^{201}Hg (2). If this light is linearly polarized, then only an alignment distribution is established. If it is circularly polarized, then the distribution is predominantly an orientation distribution, with a small alignment moment. These longitudinal distributions are rotated into a transverse distribution by means of a transverse oscillatory magnetic field at the Larmor frequency, applied through the AC coils shown in Figure 1.1. In these experiments, the H_0 field was about 1.3 and 3.5 gauss for measurements on ^{199}Hg and ^{201}Hg , respectively, which corresponds to a Larmor frequency of 975 Hz.

Relaxation times usually are determined by establishing a transverse orientation distribution and by then simultaneously shutting off both the pump beam and the transverse magnetic field. If no quadrupole perturbation is present, the signal decays exponentially. The relaxation time, which is determined by a circuit not shown in Figure 1.1, is the time required for the signal to decay by a factor of e . A more accurate method for determining relaxation times, with no light present, was used for the cube-shaped cell and is described in Section 2.6.4.

In developing the model for the interaction which takes place on the cell wall, ^{199}Hg with a nuclear spin of $1/2$, interacts only with magnetic

THE SINGER COMPANY • KEARFOTT DIVISION

fields, while ^{201}Hg , with a spin of $3/2$, possesses an electric quadrupole moment and interacts with electric field gradients as well as with magnetic fields.

2. EFFECTS DUE TO QUADRUPOLE PERTURBATIONS

2.1 INTRODUCTION

The nucleus of ^{201}Hg has a spin of $3/2$, and can be affected by quadrupole perturbations from various sources. Such perturbations can affect the relaxation of the nuclear spins, as well as their steady-state free precession.

A quadrupole perturbation is a small change in the magnetic energy levels of a system with a spin greater than one half. It has two properties of interest: energy levels with different values of $|m|$ have different shifts in energy, and the strength of the perturbation V varies with the angle θ between the perturbation symmetry axis and the quantization direction:

$$V \propto \frac{1}{2}(3\cos^2\theta - 1) = P_2(\cos\theta) \quad (2.1.1)$$

where $P_2(\cos\theta)$ is a second-order Legendre polynomial. Note that V changes sign as θ is varied from 0° to 90° , passing through $V = 0$ at $\theta = 54.74^\circ$, and that $V(\theta) = V(-\theta)$.

A quadrupole perturbation also causes a torque T , which is given by the derivative of V with respect to θ :

$$T \propto \cos\theta\sin\theta \propto \sin 2\theta \quad (2.1.2)$$

The torque is zero at $\theta = 0^\circ$ and at $\theta = 90^\circ$, but not at $\theta = 54.74^\circ$.

A rigorous quantum-mechanical description of a quadrupole perturbation yields terms proportional to the energy shift and to the torque, along

with a third term whose classical analog is less clear. This term can couple magnetic energy levels whose quantum numbers m differ by two, and it varies with angle as $\sin^2\theta$. An admittedly vague classical analog of this term can be given in terms of the precessional motion of a spin in a quadrupole field. If the spin precesses about the axis of the quadrupole field ($\theta=0^\circ$), its motion can be completely described by functions which are periodic with respect to a single frequency, ω . If it precesses about an axis which is perpendicular to that of the quadrupole field ($\theta=90^\circ$), a description of its motion requires functions with a periodicity of 2ω as well as functions with a periodicity of ω . The third term in the quadrupole perturbation is related to the amount of this second-harmonic content in the precessional motion of the spin. It will be called the "2 ω " term in the discussion below.

The angular dependences of these three terms is illustrated in Figure 2.1.1.

In the past, only the effects of the shift in the average energy levels^(1,5) have been studied. These effects include beats in the decay signals of ^{201}Hg in the presence of a steady-state quadrupole perturbation. During the current reporting period, theoretical models for quadrupole perturbations were improved, and some of the predictions of these improved models were tested experimentally. This chapter of this interim report describes the origins of such perturbations, the theoretical method which was used to predict their effects, and the experimental tests of these predictions.

2.2 SOURCES OF QUADRUPOLE PERTURBATIONS

There are two major sources of quadrupole perturbations in mercury magnetic resonance experiments: interactions with the cell wall, and interactions with the optical-pumping and readout light. Understanding the interactions between the mercury nuclei and the cell wall is the primary goal of this investigation. The interactions with the light beams often cause a much stronger quadrupole perturbation, which is more easily

— Energy Shift
- - - Torque
..... 2ω

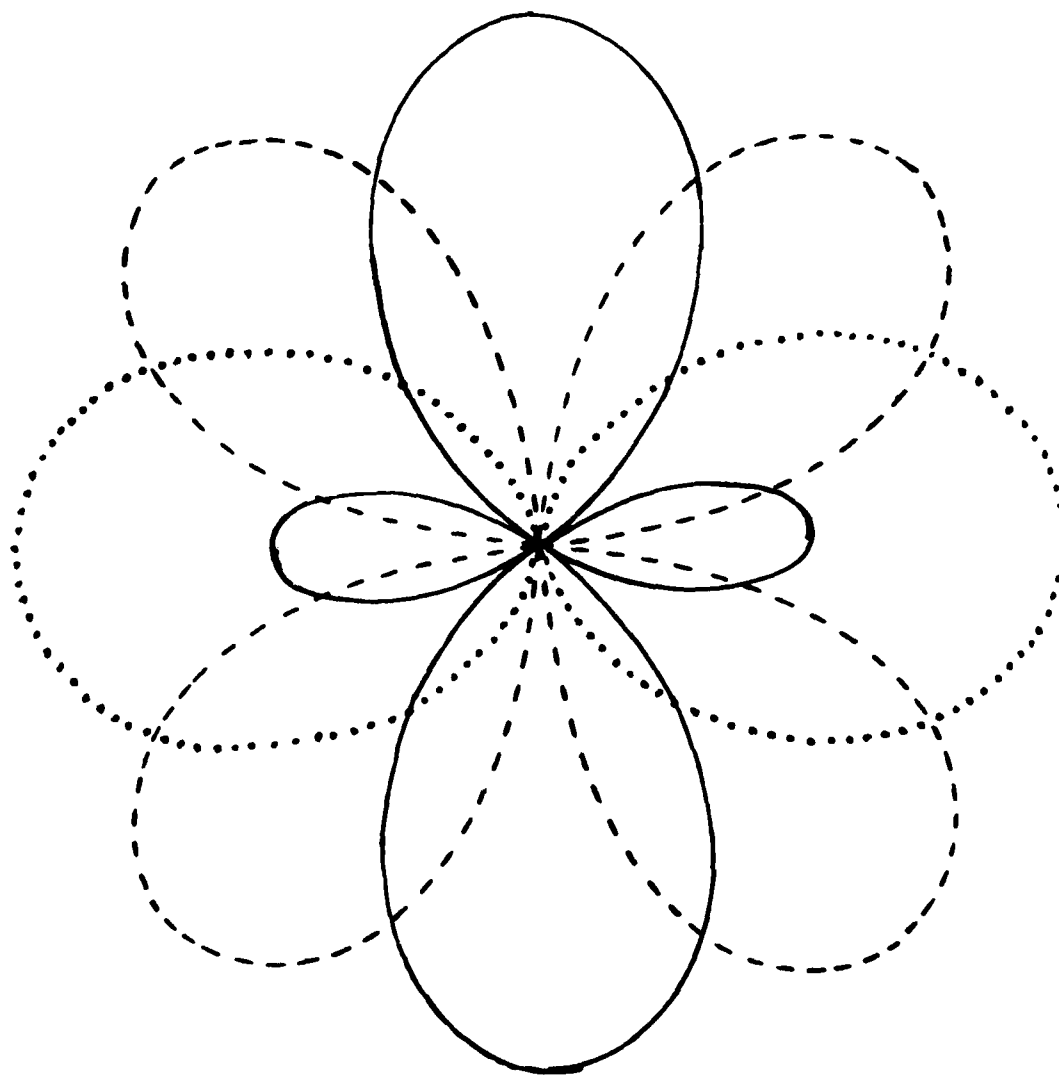


FIGURE 2.1.1 - Angular Dependence of Quadrupole Terms (Arbitrary Scale)

observed and quantified. Both types of perturbations will be described in this section.

2.2.1 Perturbations Due to the Cell Wall

The nucleus of ^{201}Hg has an electric quadrupole moment, and therefore a quadrupole perturbation can arise from the effects of an electric field gradient at the nucleus. Such a field gradient exists whenever the mercury atom is adsorbed onto the cell wall, regardless of the mechanism for adsorption. If an atom is adsorbed onto a surface, then there must be an electric field pulling it back toward the surface if it moves away, pushing it away from the surface if it gets too close, and equal to zero at the equilibrium distance from the surface (see Figure 2.2.1). Therefore, the electric field has a gradient normal to the surface. A weakly adsorbed atom such as mercury on fused silica is usually free to hop about the surface, which indicates that any electric field gradients parallel to the surface are much weaker than the component normal to the surface.

The quadrupole moment Q of the nucleus is defined by

$$eQ = \int_{\text{volume of nucleus}} \rho r^2 (3\cos^2\theta - 1) dV \quad (2.2.1)$$

where e is the magnitude of the electronic charge ($e > 0$), ρ is the charge density within the nucleus, and the integral is to be done for the nucleus in the $m = +I$ state (i.e., $m = +3/2$ for ^{201}Hg). The quadrupole moment of the nucleus is positive⁽⁴⁾, which indicates that the nucleus is cigar-shaped, with the cigar parallel to the quantization direction when $m = +3/2$. If this cigar-shaped distribution is placed in the electric field gradient described above, it will tend to orient its axis

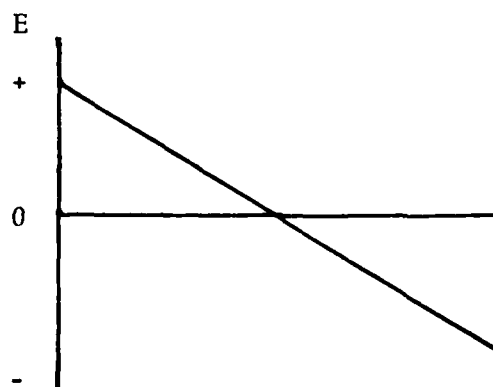
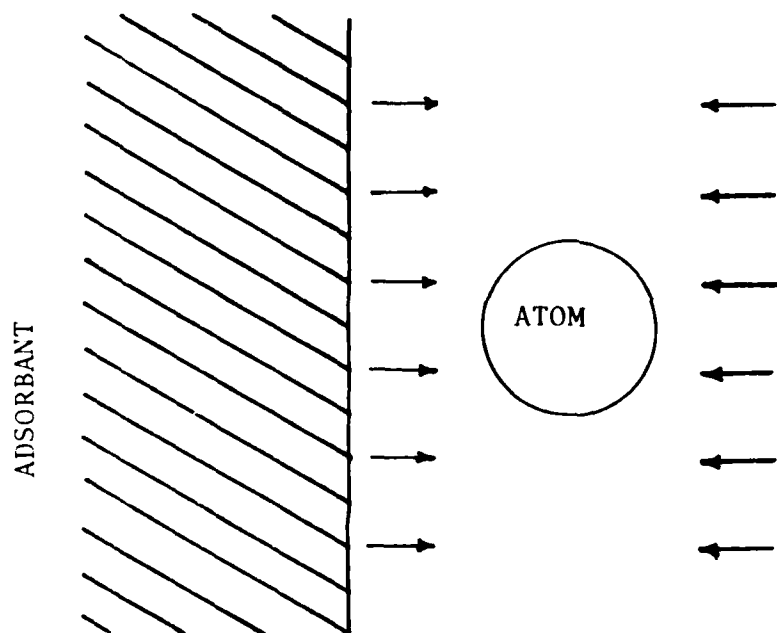


FIGURE 2.2.1 - Electric Field Near an Adsorbed Atom

perpendicular to the field gradient axis. If the quantization axis is parallel to the field gradient axis ($\theta=0^\circ$), then this orientation corresponds to a linear combination of $m = \pm 1/2$ states, and it indicates that the $\pm 3/2$ states have the higher energy. This corresponds to a positive quadrupole perturbation, which for a spin $3/2$ particle is defined as a perturbation which raises the $\pm 3/2$ levels relative to the $\pm 1/2$ levels at $\theta = 0$.

A polarized atom is adsorbed and desorbed many times before it is relaxed, and it therefore samples the entire cell surface. This results in a randomly fluctuating perturbation. If the strength of the field gradient is uniform over the entire cell wall, then it can be shown that both the energy shift term and the torque term average to zero over a cell which is a perfect sphere or a perfect cube. The 2ω term does not average to zero. A slight departure from these shapes, caused, for instance, by the sealoff tip, can result in a non-zero average value for the energy shift and torque terms as well, which implies a steady-state perturbation. The effects of this non-zero average energy shift have been studied previously^(1,5).

In summary, the forces which cause adsorption on the cell wall also give rise to an electric field gradient at the nucleus, which causes a quadrupole perturbation on ^{201}Hg . The axis of this field gradient (and, therefore, of the perturbation) is directed normal to the surface. The average value of this randomly fluctuating perturbation is determined in part by the geometry and the orientation of the cell.

2.2.2 Perturbations Due to Light

The fact that uv light near 253.7nm can shift the energy levels of mercury has been verified theoretically and experimentally.⁽⁶⁾ This shift occurs because the uv light can couple the ground state to the excited state, and this coupling tends to shift the energies of the various magnetic

levels in both states. If the shifts for the $^{201}\text{Hg } m = \pm 3/2$ levels are not equal to the shift for the $m = \pm 1/2$ levels, then a quadrupole perturbation will result. It can be shown that this perturbation also has the torque and the 2ω terms. Since this light-induced perturbation is stronger and is more easily controlled experimentally than the cell-wall-induced perturbation, it is useful in experiments for detection and measurement of the effects of quadrupole perturbations.

2.2.3 Consistency of the Algebraic Signs of the Perturbations

If the torque and the 2ω terms are neglected, then the combined effect of quadrupole perturbations from two sources is simply the algebraic sum of the energy-shift terms. If the two perturbations have energy-shift terms which are equal in magnitude but opposite in sign, then the net energy-shift term is zero. As described above, the perturbation due to the electric field gradient on the cell wall is proportional to $+P_2(\cos\theta_1)$, where θ_1 is the angle between the quantization direction (determined by the external magnetic field) and the axis of the average quadrupole perturbation due to the cell wall. The theory of light-induced energy shifts predicts that linearly polarized uv light from a ^{202}Hg lamp, directed perpendicular to the quantization direction, causes a perturbation which is proportional to $-P_2(\cos\theta_2)$, where θ_2 is the angle between the polarization and quantization directions. Suppose the perturbations from these two sources cancel each other for a certain pair of values of θ_1 and θ_2 . If θ_1 is increased, then θ_2 must also be increased in order for the perturbations to cancel each other again, since $P_2(\cos\theta)$ is a monotonic function of θ for $0^\circ \leq \theta \leq 90^\circ$. Preliminary experiments, which detected the presence of a net quadrupole perturbation by looking for a non-exponential decay (Section 2.4) confirm this relationship between θ_1 and θ_2 . Since the two perturbations arise from different types of mechanisms, these results strongly support the descriptions for both the cell-wall-induced and the light-induced quadrupole perturbations.

2.3 DENSITY MATRIX AND SPHERICAL BASIS OPERATORS

In the calculations described in this Chapter, as well as in most calculations of the effects due to perturbations, the nuclear spin distribution is described in terms of a density matrix ρ , defined by

$$\rho = \sum_{mm'} \rho_{mm'} |m\rangle\langle m'|, \quad (2.3.1)$$

where $|m\rangle$ are basis states with a z-component of angular momentum m . The density matrix has the property that the expectation value $\langle I \rangle$ of any observable I is found by multiplying the corresponding operator I_{op} by ρ and taking the trace:

$$\langle I \rangle = \text{Tr}(I_{op} \rho). \quad (2.3.2)$$

The observables of interest are the signals observed using either the rotation of linearly polarized readout light or the change of ellipticity of elliptically polarized readout light. The corresponding operators are, respectively,

$$I_L = I_x = \text{Re}(I_+) \quad (2.3.3)$$

and

$$I_E = \text{Im}(I_z I_+ + I_+ I_z), \quad (2.3.4)$$

where I_x , I_z , and I_+ are angular momentum operators.

Two types of spin distributions have been considered. A longitudinal distribution has all spins parallel to the static magnetic field H_0 . Such a distribution can be established using optical pumping, with the light along the H_0 direction. A transverse distribution has a component of spin perpendicular to H_0 , and can be established, for instance, by applying

a transverse magnetic field to a longitudinal distribution. When no transverse field is present, the transverse component of the spin magnetic moment precesses around the H_0 direction at the Larmor frequency, and can be detected by the readout light described above.

The time-dependence of ρ is given by

$$\frac{d\rho}{dt} = -\frac{i}{\hbar} [\mathcal{H}, \rho], \quad (2.3.5)$$

and a solution for this equation is

$$\rho(t) = e^{(-i/\hbar)\mathcal{H}t} \rho(0) e^{(i/\hbar)\mathcal{H}t} \quad (2.3.6)$$

where \mathcal{H} is the total Hamiltonian for the system.

It is possible to perform the calculation of $\rho(t)$ using the density matrix as expressed in equation (2.3.1); however, this leads to very complicated algebraic expressions. A much simpler method is to express the density matrix, the Hamiltonian, and the operators corresponding to observables in terms of spherical basis operators T_{LM} , defined by⁽⁷⁾

$$T_{LM} = \sum_m |m\rangle \langle m-M| (-1)^{m-M-K} C(KKL; m, M-m) \quad (2.3.7)$$

where K is the total spin of the atom ($K = 3/2$ for ^{201}Hg), and $C(KKL; m, M-m)$ is a Clebsch-Gordan coefficient. Specifically, for $K=3/2$,

$$T_{00} = \frac{1}{2} \sum_m |m\rangle \langle m| = \frac{1}{2} \mathbf{1}, \quad (2.3.8a)$$

$$T_{10} = \frac{1}{\sqrt{5}} \sum_m m |m\rangle \langle m| = \frac{1}{\sqrt{5}} I_z, \quad (2.3.8b)$$

$$\begin{aligned}
 T_{1,\pm 1} &= \mp \frac{1}{\sqrt{10}} [\sqrt{3}|\pm 3/2\rangle\langle \pm 1/2| + 2|\pm 1/2\rangle\langle \mp 1/2| + \sqrt{3}|\mp 1/2\rangle\langle \mp 3/2|] \\
 &= \mp \frac{1}{\sqrt{10}} I_{\pm} ,
 \end{aligned} \tag{2.3.8c}$$

$$\begin{aligned}
 T_{2,\pm 1} &= - \frac{1}{\sqrt{2}} [\sqrt{3}|\pm 3/2\rangle\langle \pm 1/2| - |\mp 1/2\rangle\langle \mp 3/2|] \\
 &= \mp \frac{1}{2\sqrt{6}} (I_z I_{\pm} + I_{\pm} I_z) ,
 \end{aligned} \tag{2.3.8d}$$

etc., where the definitions of I_z and I_{\pm} have been used:

$$I_z |m\rangle = m|m\rangle \tag{2.3.9}$$

or

$$I_z = \sum_m m|m\rangle\langle m|$$

and

$$I_{\pm} |m\rangle = ((3/2 \mp m)(5/2 \pm m))^{1/2} |m\pm 1\rangle \tag{2.3.10}$$

or

$$I_{\pm} = \sqrt{3} |\pm 3/2\rangle\langle \pm 1/2| + 2|\pm 1/2\rangle\langle \mp 1/2| + \sqrt{3}|\mp 1/2\rangle\langle \mp 3/2|.$$

The T_{LM} 's obey the orthonormality relationship

$$\text{Tr}(T_{LM} T_{L'M'}) = \delta_{LL'} \delta_{M-M'} (-1)^M. \tag{2.3.11}$$

Therefore, if the density matrix is expressed as a linear combination of the T_{LM} 's, using the phase convention of Happer or Rose⁽⁷⁾,

$$\rho = \sum_{L,M} (-1)^M \rho_{L,M} T_{L,-M} \quad (2.3.12)$$

then the evaluation of expectation values of observables becomes very simple. For instance,

$$\begin{aligned} I_z &= \text{Tr}(I_z \rho) \\ &= \text{Tr}((\sqrt{5} T_{10}) (\sum_{L,M} (-1)^M \rho_{LM} T_{L,-M})) \\ &= \sqrt{5} \rho_{10} \end{aligned} \quad (2.3.13)$$

and

$$\begin{aligned} I_L &= \text{Re}(I_+) = \text{Re}(\text{Tr}(I_+ \rho)) \\ &= \text{Re}(\text{Tr}((-\sqrt{10} T_{1,1}) (\sum_{L,M} (-1)^M \rho_{LM} T_{L,-M}))) \\ &= \sqrt{10} \text{Re}(\rho_{11}). \end{aligned} \quad (2.3.14)$$

Similarly,

$$I_E = \text{Im}(I_z I_+ + I_+ I_z) = 2\sqrt{6} \text{Im}(\rho_{21}). \quad (2.3.15)$$

Therefore, when the density matrix is expressed by equation (2.3.12), the rotation readout signal will be proportional to $\text{Re}(\rho_{11})$, and the elliptically polarized readout signal will be proportional to $\text{Im}(\rho_{21})$.

The T_{LM} 's obey the commutation relation⁽⁸⁾

$$[T_{LM}, T_{L'M'}] = \sum_{L''} T_{L'', M+M'} [(2L+1)(2L'+1)]^{1/2} \quad (2.3.16)$$

$$\times W(LL'KK; L''K) C(LL'L''; -MM') [(-1)^{L+L'+L''} - 1].$$

This expression is not as formidable as it might appear to be, since many of the terms in the summation over L'' are zero, and since the Racah coefficients $W(LL'KK; L''K)$ and the Clebsch-Gordan coefficients can be obtained from tables in the literature⁽⁹⁾. Therefore, equation (2.3.16) can be used to solve equation (2.3.5), which leads to a set of coupled differential equations for the density matrix elements $\rho_{LM}(t)$. In many cases, these differential equations can be solved, and the solutions yield directly the time dependence of the observables of interest. This method was used to evaluate the ^{201}Hg decay transients (Section 2.4) and the steady-state solutions in the presence of a transverse rf magnetic field (Section 2.5), and in conjunction with second-order perturbation theory, to evaluate relaxation rates due to an anisotropic quadrupole perturbation (Section 2.6).

2.4 NON-EXPONENTIAL DECAY

Non-exponential relaxation of the transverse magnetic moment of an optically-pumped spin distribution has been reported for nuclei such as ^{201}Hg ⁽¹⁾ and ^{83}Kr ⁽¹⁰⁾, which have spins of 3/2, but not for spin 1/2 nuclei such as ^{199}Hg or ^{129}Xe . This departure from exponential decay has been explained in terms of a quadrupole perturbation, which affects only nuclei with a spin greater than 1/2. Calculations which have been reported in the past have modelled the effect of the perturbation as a splitting of the spin-3/2 resonance into three separate frequencies⁽¹⁾ or have calculated the effect of the perturbation in terms of a 4x4 density matrix. Although these calculations were able to explain correctly the observed nonexpo-

nential decay, they do not reveal directly other effects of a quadrupole perturbation, such as its effect on the transverse alignment moment or on longitudinal orientation and alignment moments. This section describes a calculation of such effects using spherical basis operators, a method which yields explicit expressions for signals observed from any transverse or longitudinal distribution. The calculation is specialized to the case of a spin 3/2 nucleus such as ^{201}Hg or ^{83}Kr .

The results described in this section are presented in greater detail in an unpublished Singer Company, Kearfott Division Technical Report⁽¹¹⁾.

2.4.1 Theory

The method described in section 2.3 is followed here, with both the density matrix ρ and the Hamiltonian \mathcal{H} expressed in terms of spherical basis operators T_{LM} . If the spins are in free precession with a Larmor frequency ω_0 , and are subject to a quadrupole perturbation with an energy $\hbar\omega_Q$, then, for $K = 3/2$, the Hamiltonian \mathcal{H} is given by

$$\mathcal{H} = \hbar\omega_0 (\sqrt{5} T_{10}) + \hbar\omega_Q T_{20}. \quad (2.4.1)$$

The terms in the quadrupole perturbation proportional to T_{21} and T_{22} have been omitted. This corresponds to the case where the angle between the perturbation axis and the quantization direction is zero (see Section 2.1). Analytic solutions have not yet been found for the general case of T_{21} , T_{22} non-zero.

As described in Section 2.3, a set of coupled differential equations is obtained. In the present case, the equations can be separated into subsets according to the value of M .

For $M = 0$, the equations are

$$\frac{d}{dt} \rho_{L0} = 0, \quad L = 1, 2, 3, \quad (2.4.2)$$

which indicates that the longitudinal moments do not become time-dependent in the presence of a quadrupole perturbation.

For $M = 1$,

$$\frac{d}{dt} \rho_{11} = i\omega_0 \rho_{11} + i\omega_Q \sqrt{3/5} \rho_{21}, \quad (2.4.3a)$$

$$\frac{d}{dt} \rho_{21} = i\omega_Q \sqrt{3/5} \rho_{11} + i\omega_0 \rho_{21} + i\omega_Q \sqrt{2/5} \rho_{31}, \text{ and} \quad (2.4.3b)$$

$$\frac{d}{dt} \rho_{31} = i\omega_Q \sqrt{2/5} \rho_{21} + i\omega_0 \rho_{31}. \quad (2.4.3c)$$

These can be solved by setting

$$\rho_{L1} = e^{i\omega_0 t} (\rho_L^0 + \rho_L^C \cos \omega_Q t + \rho_L^S \sin \omega_Q t), \quad L = 1, 2, 3, \quad (2.4.4)$$

and by applying the boundary conditions at $t = 0$:

$$\rho_{L1}(0) = \rho_L^0 - \rho_L^C, \quad L = 1, 2, 3. \quad (2.4.5)$$

The result is:

$$\begin{aligned} \rho_{11}(t) = & \frac{2+3\cos \omega_Q t}{5} \rho_{11}(0) + i\sqrt{3/5} \sin \omega_Q t \rho_{21}(0) \\ & + \frac{\sqrt{6}}{5} (\cos \omega_Q t - 1) \rho_{31}(0), \end{aligned} \quad (2.4.6a)$$

$$\begin{aligned} \rho_{21}(t) = & i\sqrt{3/5} \sin \omega_Q t \rho_{11}(0) + \cos \omega_Q t \rho_{21}(0) \\ & + i\sqrt{2/5} \sin \omega_Q t \rho_{31}(0), \text{ and} \end{aligned} \quad (2.4.6b)$$

$$\begin{aligned} \rho_{31}(t) = & \frac{\sqrt{6}}{5} (\cos \omega_Q t - 1) \rho_{11}(0) + i \sqrt{2/5} \sin \omega_Q t \rho_{21}(0) \\ & + \frac{3 + 2 \cos \omega_Q t}{5} \rho_{31}(0). \end{aligned} \quad (2.4.6c)$$

These equations do not take into account the exponential relaxation of the spin distribution due, for instance, to interactions with the walls of the container. The relaxation can be included⁽¹³⁾ by rewriting equation (2.3.5) as

$$\frac{d\rho}{dt} = \frac{i}{\hbar} [\mathcal{H}, \rho] - \left. \frac{d\rho}{dt} \right|_{\text{relaxation}} \quad (2.4.7)$$

In many cases, each component ρ_{LM} relaxes exponentially with a relaxation time τ_L . The effect of including this relaxation in the calculation is that the terms $\rho_{L1}(0)$ are replaced by terms $\rho_{L1}(0) e^{-t/\tau_L}$, for $L = 1, 2, 3$.

In the presence of a quadrupole perturbation, two effects are noted: 1) the normal orientation and alignment signals show "beats", and 2) the signals from the normally unobserved distributions appear, 90° out of phase with the "normal" signal. Beats in the free precession decay of orientation signals for spin $3/2$ atoms have been reported^(1,10). In those experiments, the quadrupole perturbation resulted from asymmetry of the cell which contained the atomic vapor. In reference 1, the orientation signals for the unperturbed system were interpreted as the sum of three orientation signals at the same frequency, arising from three two-level systems ($|3/2\rangle \rightarrow |1/2\rangle$, $|1/2\rangle \rightarrow |-1/2\rangle$, $|-1/2\rangle \rightarrow |-3/2\rangle$) all with the same energy difference between levels. The quadrupole perturbation then caused a slight shift in the $|\pm 1/2\rangle$ energy levels relative to the $|+5/2\rangle$ levels, which caused the three signals to be split into three slightly different frequencies. This frequency splitting was observed as beats in the amplitude of the orientation signals.

This same picture can be used to explain the appearance of an alignment signal during free precession of an initially pure orientation distribution. Figure 2.4.1a-3a shows three spins, corresponding to the three two-level systems, at $t = 0$, when their distribution has an orientation moment along the x-axis and has no alignment moment. Figure 2.4.1b shows these same spins at $t = N\pi/\omega_0$, where $N\pi\omega_0/\omega_1 \gg 1$. The quadrupole perturbation has caused the spins to precess at different rates, and their distribution now has an alignment moment (along the y-axis) as well as an orientation moment (along the x-axis). Later, as in Figure 2.4.1c, the orientation moment disappears, while the alignment moment is still non-zero.

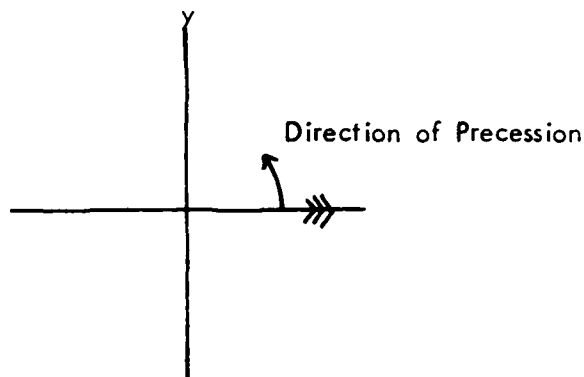
It was shown above (equation 2.4.2) that the density matrix elements corresponding to a longitudinal orientation or alignment distribution do not change in the presence of a quadrupole perturbation. Therefore, no additional time dependence is introduced. The model of three two-level systems, described in the previous section, provides a simple physical picture for this lack of change under a quadrupole perturbation. When the spins are aligned parallel to H_0 , they do not precess. Therefore there are no oscillatory signals whose frequencies can be split, and the mechanism shown in Figure 2.4.1 does not occur.

In the absence of a quadrupole perturbation ($\omega_Q = 0$), equations 2.4.6 show that the rotation of the linearly polarized light is determined only by the transverse orientation distribution, and the change in ellipticity of elliptically polarized light only by the transverse alignment distribution, as mentioned above. The equations also suggest that an octupole moment distribution, once established, can, in principle, be detected using optical readout of the free spin precession in the presence of a quadrupole perturbation.

a: $t = 0$

Orientation $\neq 0$

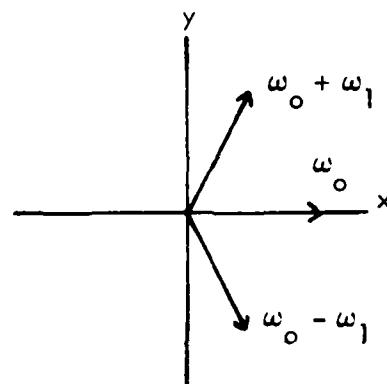
Alignment $= 0$



b: $t = N\pi/\omega_0 \approx 1/\omega_1$

Orientation $\neq 0$

Alignment $\neq 0$



c: $t = (2\pi/3)/\omega_1$

Orientation $= 0$

Alignment $\neq 0$

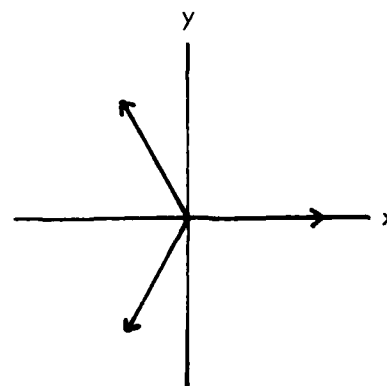


FIGURE 2.4.1 - ^{201}Hg Free Precession Described Using Three Independent Spins

2.4.2 Experimental

The spin distributions were established and monitored using the Faraday readout apparatus described in Section 1.2. The switching circuit for the transverse magnetic field was connected to the pump beam shutter so that the pump beam and the transverse field could be shut off simultaneously, after which the nuclear spins were in free precession, affected by only the H_0 field and the quadrupole perturbation. In these experiments, the perturbation was the result of unequal readout-light-induced frequency shifts for the $|\pm 3/2\rangle$ and $|\pm 1/2\rangle$ sublevels of ^{201}Hg . (see Section 2.2.2). Similar but weaker effects have been observed for quadrupole perturbations caused by interactions with the cell wall.

A typical decay curve for an orientation distribution (circularly polarized pumping light) is shown in Figure 2.4.2, along with the results of a least-squares fit to the first term in equation (2.4.6a). There is good agreement between theory and experiment except for the second peak (between 60 and 100 seconds). No improvement was obtained by a fit to the sum of the first and second or of the first and third terms of equation (2.4.6a), indicating that the observed signals were due only to an orientation distribution.

Results for an alignment distribution (linearly polarized pumping light) are shown in Figure 2.4.3. A pure alignment moment should yield no signal until after the transverse magnetic field has been turned off. The observed nonzero signal at $t = 0$ is probably due to the presence of an orientation moment along with the alignment moment. Two possible causes for such an orientation moment are: 1) optically active components in the pump beam, which result in slightly elliptically polarized pumping light, and 2) the combined interaction of the transverse magnetic field and the quadrupole perturbation, which can be shown to produce a transverse orientation moment even in the presence of purely linearly polarized pumping light. The experimental data were least-squares fitted to the sum of the

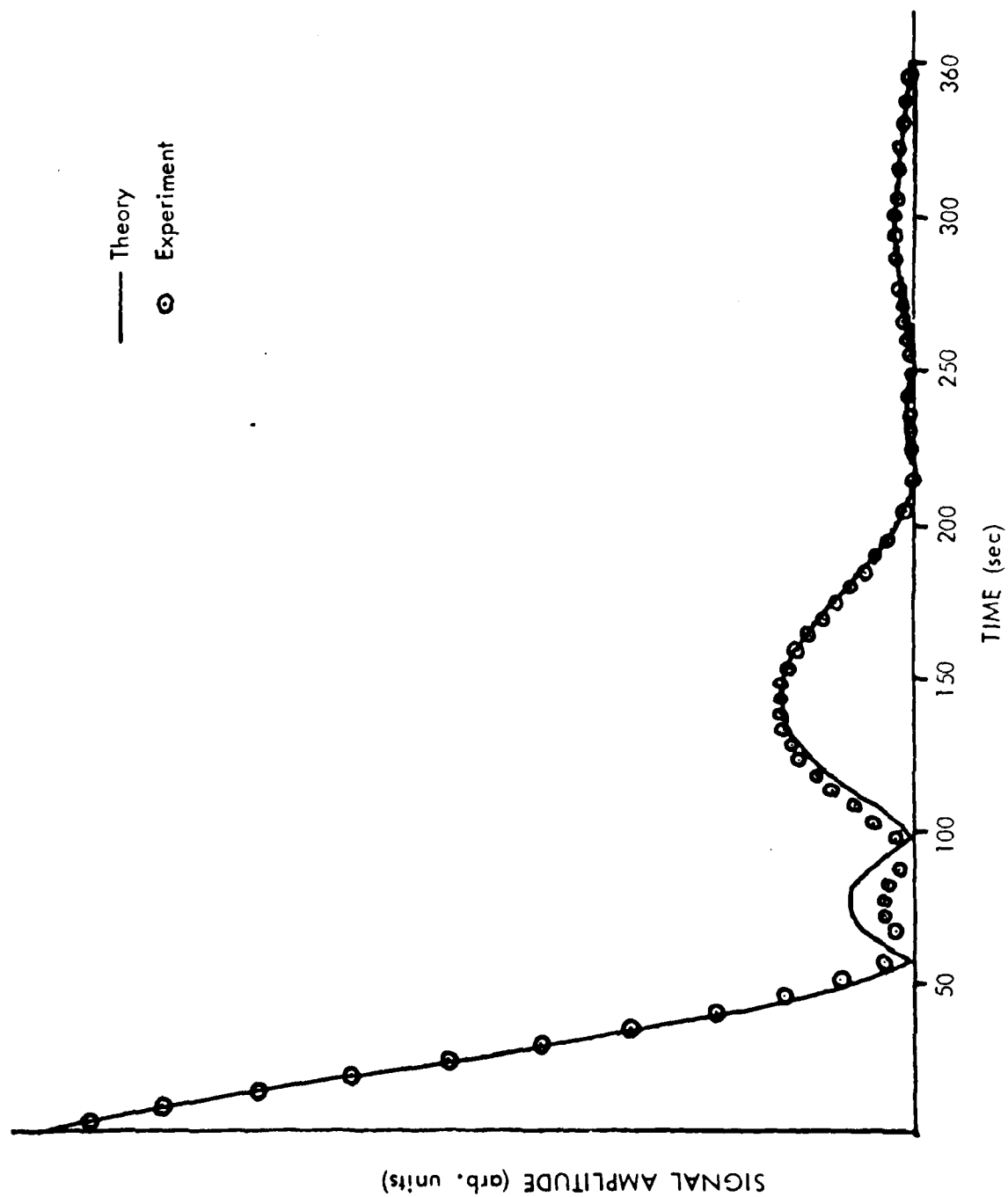


FIGURE 2.4.2 - Free-Precession Decay Transient of ^{201}Hg Orientation Signal

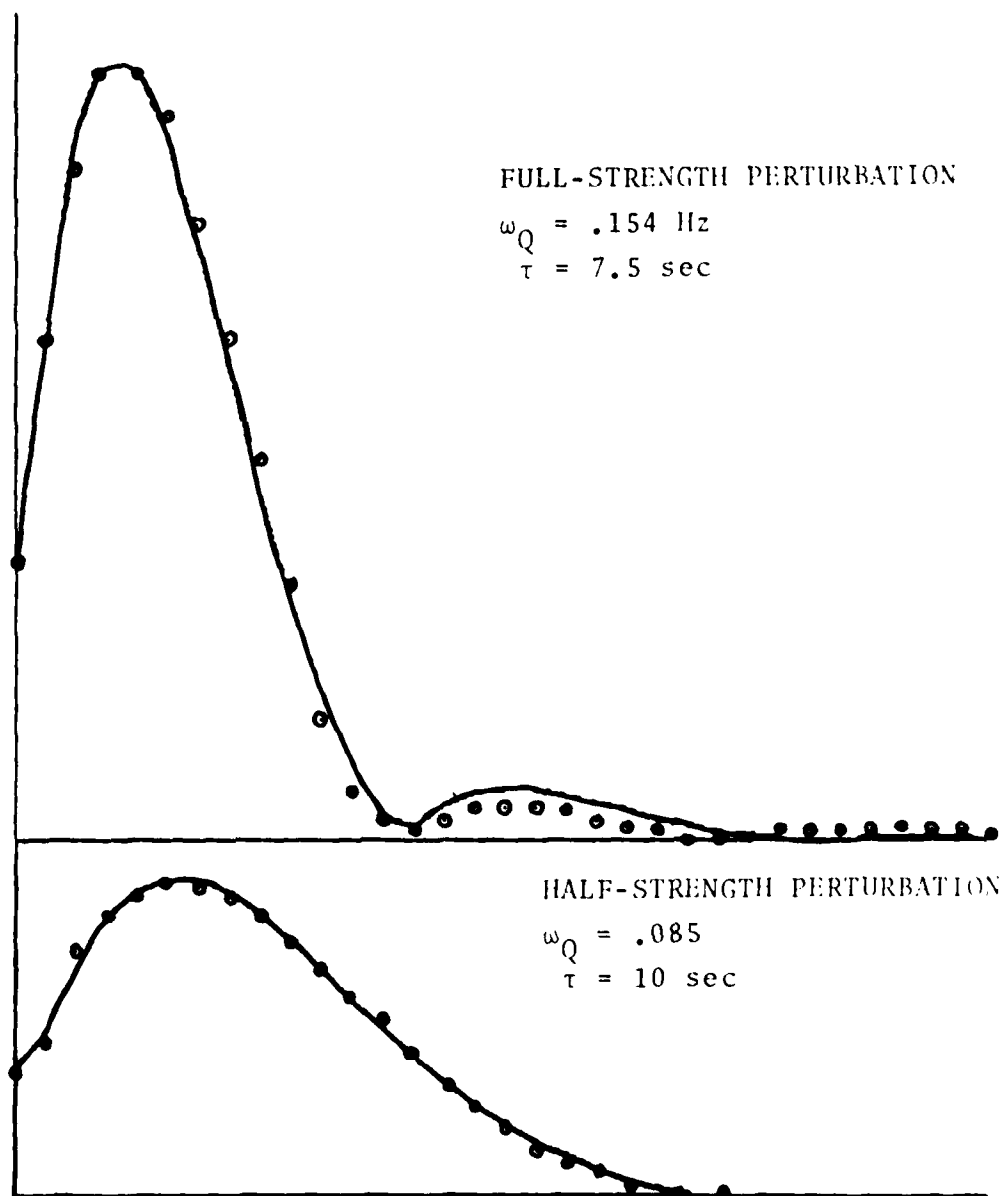


FIGURE 2.4.3 - Free-Precession Decay Transient of ^{201}Hg
Alignment Signal and Values of Fitted
Parameters

first and second terms in equation (2.4.6b), and reasonable agreement was obtained. Note that the fitted value of ω_Q in Figure 2.4.3 is reduced by approximately one half when the readout light intensity, which is the source of the quadrupole perturbation, is reduced by one half, in agreement with the proportionality of the light intensity, the light-induced quadrupole perturbation, and the "beat frequency" of the decay transients. The shorter relaxation time for the upper trace is due to the increased relaxation caused by the full-strength readout light.

The calculations described above yield explicit expressions for the time dependence of a freely precessing spin distribution in the presence of a quadrupole perturbation, and they show in a concise manner how the various transverse moments are coupled by such a perturbation. The calculations were done explicitly for a spin 3/2 system, but the method could be applied easily to other values of spin, since this value enters the calculation only through the commutation relation for the T_{LM} 's (equation 2.3.16) and the coefficients in the expression for the Hamiltonian (equation 2.4.1).

2.5 COMBINED QUADRUPOLE PERTURBATION/TRANSVERSE MAGNETIC FIELD/PUMPING RADIATION/RELAXATION

The situation is frequently encountered where the mercury nuclei are subjected to the combined effects of a steady-state magnetic field H_0 , a transverse rf magnetic field H_1 , a quadrupole perturbation, optical pumping radiation, and relaxation on the cell walls. The time dependence of the density matrix ρ is then given by

$$\frac{d\rho}{dt} = -\frac{i}{\hbar} [(\mathcal{H}_0 + \mathcal{H}_1 + \mathcal{H}_Q), \rho] + \left. \frac{d\rho}{dt} \right|_{\text{pump}} + \left. \frac{d\rho}{dt} \right|_{\text{relaxation}} \quad (2.5.1)$$

where the terms \mathcal{H}_0 , \mathcal{H}_1 , and \mathcal{H}_Q are the Hamiltonians corresponding to the H_0 and H_1 magnetic fields and to the quadrupole perturbation, respectively and are given by

$$\mathcal{H}_0 = \hbar\omega_0 I_z = \hbar\omega_0 \sqrt{5} T_{10}, \quad (2.5.2)$$

$$\mathcal{H}_1 = \hbar\omega_1 e^{-i\omega_a t I_z} (I_x) e^{i\omega_a t I_z} \quad (2.5.3)$$

$$= \sqrt{5/2} \hbar\omega_1 e^{-i\omega_a t \sqrt{5} T_{10}} (T_{1,-1} - T_{1,1}) e^{i\omega_a t \sqrt{5} T_{10}}, \text{ and}$$

$$\mathcal{H}_Q = \hbar\omega_Q \text{ for } m = \pm 3/2; -\hbar\omega_Q \text{ for } m = \pm 1/2 \quad (2.5.4)$$

$$= \hbar\omega_Q T_{20}.$$

In the above equations, ω_0 is the Larmor frequency, ω_1 is proportional to the strength of the rf magnetic field ($\omega_1 = \gamma H_1$, where γ is the gyro-magnetic ratio), ω_a is the frequency of the rf magnetic field, and ω_Q is proportional to the strength of the quadrupole perturbation. The terms of the quadrupole perturbation proportional to T_{21} and T_{22} have been neglected in this calculation. This implies either that the quadrupole axis is parallel to H_0 (where these terms are zero) or that only first-order perturbation is assumed.

The last two terms in equation (2.5.1) are assumed to be given by

$$\frac{d\rho_{LM}}{dt} \Big|_{\text{pump}} + \frac{d\rho_{LM}}{dt} \Big|_{\text{relaxation}} = -\frac{1}{\tau_L} (\rho_{LM} - R_{LM}), \quad (2.5.5)$$

where τ_L is the relaxation time for a spin distribution with multipolarity L , and R_{LM} is the steady-state value of ρ_{LM} due to optical pumping when no

transverse field is present. An orientation distribution has $L = 1$ and an alignment distribution has $L = 2$. Also, R_{LM} is zero unless M is zero, for the case where optical pumping produces a longitudinal distribution.

The time dependence of the density matrix can be found using the method described in Section 2.3. The result is fifteen coupled differential equations with the fifteen variables $\rho_{LM}(t)$ for $L = 0$ to 3 and $M = 0$ to L , which are listed explicitly in Figure 2.5.1. The steady-state solutions can be assumed to have the form

$$\rho_{LM}(t) = e^{iM\omega_a t} \rho_{LM} \quad (2.5.6)$$

where ρ_{LM} is now used to designate the steady-state magnitudes of the various density matrix elements. These solutions are then substituted into the coupled differential equations, which then can be simplified to a set of simultaneous equations for the time-independent variables ρ_{LM} . These equations are too cumbersome to solve analytically, but numerical solutions can be obtained easily using a digital computer. This was done for various values of ω_1 , ω_a , R_{LM} , and $\Delta\omega$, where $\Delta\omega = \omega_a - \omega_0$.

Before solving these equations, several items should be noted:

1. The quadrupole perturbation is the only coupling between states of different L . Therefore the orientation and alignment moments do not affect one another when ω_Q is zero.
2. The transverse H_1 magnetic field is the only coupling between states of different M . In the absence of such a field, the longitudinal and transverse moments are independent.

In many experiments, the NMR signals are obtained by using the Faraday readout signal to drive the transverse H_1 magnetic field (see, for

$$\frac{d}{dt} \rho_{10} + \frac{1}{\tau_1} \rho_{10} + \frac{i\omega_1}{\sqrt{2}} (e^{-i\omega_0 t} \rho_{11} + e^{i\omega_0 t} \rho_{1-1}) = \frac{1}{\tau_1} R_{10}$$

$$\frac{d}{dt} \rho_{11} + \frac{i\omega_1}{\sqrt{2}} e^{i\omega_a t} \rho_{10} + (-i\omega_0 + \frac{1}{\tau_1}) \rho_{11} - i\omega_Q \sqrt{3/5} \rho_{21} = 0$$

$$\frac{d}{dt} \rho_{20} + \frac{1}{\tau_2} \rho_{20} + i\omega_1 \sqrt{3/2} (e^{-i\omega_a t} \rho_{21} + e^{i\omega_a t} \rho_{2-1}) = \frac{1}{\tau_2} R_{20}$$

$$\begin{aligned} \frac{d}{dt} \rho_{21} + i\omega_1 \sqrt{3/2} e^{i\omega_a t} \rho_{20} - i\omega_Q \sqrt{3/5} \rho_{11} + (-i\omega_0 + \frac{1}{\tau_2}) \rho_{21} + i\omega_1 e^{-i\omega_0 t} \rho_{22} \\ - i\omega_Q \sqrt{2/5} \rho_{31} = 0 \end{aligned}$$

$$\frac{d}{dt} \rho_{22} + i\omega_1 e^{i\omega_a t} \rho_{21} + (-2i\omega_0 + \frac{1}{\tau_2}) \rho_{22} - i\omega_Q \rho_{32} = 0$$

$$\frac{d}{dt} \rho_{30} + \frac{1}{\tau_3} \rho_{30} + i\omega_1 \sqrt{3} (e^{-i\omega_a t} \rho_{31} + e^{i\omega_a t} \rho_{3-1}) = \frac{1}{\tau_3} R_{30}$$

$$\frac{d}{dt} \rho_{31} + i\omega_1 \sqrt{3} e^{i\omega_a t} \rho_{30} - i\omega_Q \sqrt{2/5} \rho_{21} + (-i\omega_0 + \frac{1}{\tau_3}) \rho_{31} - i\omega_1 \sqrt{5/2} e^{-i\omega_0 t} \rho_{32} = 0$$

$$\frac{d}{dt} \rho_{32} - i\omega_Q \rho_{22} + i\omega_1 \sqrt{5/2} e^{i\omega_a t} \rho_{31} + (-2i\omega_0 + \frac{1}{\tau_3}) \rho_{32} + i\omega_1 \sqrt{3/2} e^{-i\omega_a t} \rho_{33} = 0$$

$$\frac{d}{dt} \rho_{33} + i\omega_1 \sqrt{3/2} e^{i\omega_a t} \rho_{32} + (-3i\omega_0 + \frac{1}{\tau_3}) \rho_{33} = 0$$

To get equations for $\frac{d}{dt} \rho_{L-M}$, take the equation for $\frac{d}{dt} \rho_{LM}$ and set $M \rightarrow -M$, $\omega_0 \rightarrow -\omega_0$, $\omega_a \rightarrow -\omega_a$, $\omega_Q \rightarrow -\omega_Q$, but $\omega_1 \rightarrow +\omega_1$.

FIGURE 2.5.1 - Coupled Differential Equations

example, Section 2.2.1 of reference 12). A phase difference $\Delta\phi$ between the signal and H_1 , caused, for instance, by the electronics which drives H_1 , would cause a change in the frequency of the signal. Examination of the numerical solutions of the simultaneous equations indicates that $\Delta\omega$ and $\Delta\phi$ are related approximately by

$$\Delta\omega \approx A(\omega_1)R_{20}\omega_Q (1 + B(\omega_1)\omega_Q^2) - \Delta\phi(C + D(\omega_1)\omega_Q^2 + E(\omega_1)\omega_Q^4), \quad (2.5.7)$$

where the coefficients A through E are positive and are functions of ω_1 , as well as of τ_1 , τ_2 , τ_3 , and R_{10} . Several features of this relation can be noted:

1. For $\omega_Q = 0$, equation (2.5.7) reduces to

$$\Delta\omega = -C\Delta\phi.$$

This result is also predicted by modelling the ^{201}Hg spin system and the H_1 drive as a resonator in a feedback loop. One would expect that the constant C is inversely proportional to the relaxation time τ , of the resonator.

2. For $R_{20} = 0$, the first term is zero, but there is still a dependence of $\Delta\omega$ upon ω_Q . Also, examination of the numerical solutions for ρ_{11} and ρ_{21} shows that the quadrupole perturbation produces a transverse alignment moment even if no longitudinal alignment moment is being produced by the optical pumping. At resonance ($\Delta\omega = 0$), the transverse alignment moment produced by the quadrupole perturbation is 90° out of phase with the transverse moment produced by alignment pumping.

3. For $\Delta\phi = 0$, the frequency change is proportional to the product of the alignment pumping rate and the quadrupole perturbation, when the perturbation is weak. The numerical solutions for $R_{10} = 0$ (no orientation pumping) show that the quadrupole perturbation again mixes the transverse orientation and alignment moments, and produces a transverse orientation moment which is 90° out of phase with the transverse moment produced by the orientation pumping. When the orientation pumping is not zero, these two transverse orientations moments add, yielding a net orientation moment which is out of phase with H_1 . This phase difference between H_1 and the Faraday readout signal causes a frequency shift $\Delta\omega$ in the same way that a phase shift in the electronics of the feedback loop causes a frequency shift.
4. No numerical solutions have been found for which $\Delta\omega$ is independent of ω_1 , unless ω_Q is zero or unless both R_{20} and $\Delta\phi$ are zero. This fact confirms that the response of the NMR cell to a change in H_1 amplitude is a valid check for the presence of a nonzero quadrupole perturbation.

Although the calculations described in this section do not deal directly with the relaxation of the nuclear spins on the wall, they show that a steady-state quadrupole perturbation, which can be caused by interactions between the nuclear spin and the wall, can affect the steady-state distribution of the nuclear spins.

2.6 RELAXATION DUE TO A FLUCTUATING ANISOTROPIC PERTURBATION

The relaxation of a nonthermal distribution of spins has been calculated by several authors⁽¹³⁾, but all of those calculations assumed an isotropic relaxing potential. Recent vapor-phase NMR relaxation measurements in containers of various shapes have shown the need for a theoretical treatment of relaxation caused by a potential with a fixed orientation with

respect to the static magnetic field used in such experiments. The first part of this section summarizes one of the more general calculations in the literature,⁽⁸⁾ and extends this calculation to the case of an anisotropic relaxation mechanism. The second part deals with the specific example of a spin-3/2 atom relaxing due to an electric field gradient, and the third part gives explicit expressions for relaxation of spin-3/2 atoms due to electric field gradients on the walls of cells with various shapes and orientations. The final part describes experimental results obtained using a cube-shaped cell, and compares the results to the theoretical predictions.

The reader should keep in mind that only the relaxation due to an anisotropic potential is calculated here. The relaxation rates due to isotropic mechanisms must be added to the rates predicted here in order to arrive at an estimate of the experimentally observed rates.

The results described in this section are presented in greater detail in an unpublished Singer Company, Kearfott Division Technical Report⁽¹⁴⁾.

2.6.1 Theory

This calculation follows the method of Happer⁽⁸⁾, who expresses the density matrix ρ and the randomly-fluctuating perturbation V in terms of spherical basis operators (see Section 2.3):

$$\rho = \sum_{L,M} (-1)^M \rho_{LM} T_{L,-M}, \text{ and} \quad (2.6.1)$$

$$V(t) = \sum_{L,M} (-1)^M V_{LM}(t) T_{L,-M}. \quad (2.6.2)$$

Happer makes use of the density matrix in the interaction representation, σ , which is given by

$$\sigma = e^{(i/\hbar) \mathcal{H}_0 t} \rho e^{-(i/\hbar) \mathcal{H}_0 t}. \quad (2.6.3)$$

He also assumes that V is isotropic, has a multipolarity ℓ , and has an exponential correlation function:

$$\langle V_{\ell m}(t) V_{\ell m}(t-\tau) \rangle_{av} = \left(\frac{1}{2\ell+1} \right) \delta_{m,-m} (-1)^m V^2 e^{-\tau/\tau_c} \quad (2.6.4)$$

where V^2 is the mean-squared strength of the perturbation, τ_c is the correlation time, and the symbol $\langle \rangle_{av}$ denotes an ensemble average. The general formula for the time dependence of the density matrix σ based upon second-order perturbation theory is stated in reference (8) as

$$\frac{d\sigma}{dt} = - \left\langle \int_0^\infty [V^*(t), [V^*(t-\tau), \sigma]] d\tau \right\rangle_{av} \quad (2.6.5)$$

where $V^*(t)$ is the potential in the interaction picture,

$$V^*(t) = e^{(i/\hbar) \mathcal{H}_0 t} V(t) e^{-(i/\hbar) \mathcal{H}_0 t} \quad (2.6.6)$$

for the unperturbed Hamiltonian \mathcal{H}_0 .

Happer then shows that the time dependence of the density matrix due to relaxation can be expressed as a set of equations

$$\frac{d}{dt} \sigma_{L,M} = \sum_{L'} R_{LL'}(M) \sigma_{L',M} \quad (2.6.7)$$

where

$$L' = L, L \pm 2, \dots, L \pm (2\ell - 2).$$

The fact that the relaxation couples only those elements of the density matrix with equal values of M is a consequence of axial symmetry as expressed by the $\delta_{m,-m}$ term in equation (2.6.4).

If V is no longer assumed to be isotropic, but to have cylindrical symmetry about some axis, then equation (2.6.4) must be modified slightly. The term V^2 is replaced by a term $V_{\ell m}^2$, dependent on ℓ and m :

$$\langle V_{\ell m}(t) V_{\ell m}(t-\tau) \rangle_{av} = \frac{1}{2\ell+1} \delta_{m,-m'} (-1)^m V_{\ell m}^2 e^{-\tau/\tau_c}. \quad (2.6.8)$$

The terms $V_{\ell m}^2$ are the mean-squared values of $V_{\ell m}(t)$ defined in equation (2.6.2). Also, note that

$$\sum_m V_{\ell m}^2 = V^2, \quad (2.6.9)$$

where V^2 is defined for equation (2.6.4).

The term $\delta_{m,-m'}$ is a consequence of the assumed axial symmetry of the potential⁽¹⁵⁾. It will be shown below that if this term were not present, then the randomly fluctuating potential V would be able to couple density matrix elements of different m , which is not physically reasonable. For instance, if σ_{10} and σ_{11} were coupled, then V would be able to transform a longitudinal orientation distribution into a coherently-precessing transverse orientation distribution. Such a transformation can only be made by a non-random potential, such as a transverse rf magnetic field near the Larmor frequency.

In the special case for $\ell = 2$, Cohen-Tannoudji⁽¹⁶⁾ expresses V in terms of spherical harmonics. In this case, the $\delta_{m,-m'}$ term follows from integration over the azimuthal angle ϕ . Such integration is necessary, even if the symmetry axis of the quadrupole potential has a fixed angle θ with respect to the quantization direction, since this random potential interacts with the spins at random intervals during their Larmor precession, which corresponds to random values of ϕ . (Cohen Tannoudji then integrates over the polar angle θ , since his calculation assumes an isotropic potential).

Equation (2.6.8) can be substituted into (2.6.5) to give the time dependence of the density matrix σ :

$$\frac{d\sigma}{dt} = \sum_{L,M} (-1)^M T_{L,M} \frac{d}{dt} \sigma_{L,-M} \quad (2.6.10)$$

$$= \sum_{L,M} \sum_{\mu,\mu'} (-1)^{\mu+\mu'+M} \sigma_{L,-M}$$

$$\times [T_{\ell,\mu}, [T_{\ell,\mu'}, T_{L,M}]]$$

$$\times \left\langle \int_0^\infty d\tau \exp(i\omega\mu t + i\omega\mu'(t+\tau)) V_{\ell,-\mu}(t) V_{\ell,-\mu'}(t-\tau) \right\rangle_{av}.$$

Commutation relations for the spherical basis operators are given in the appendix of reference 8. With these commutation relations, the double commutator in equation (2.6.10) above can be expressed as

$$[T_{\ell,\mu}, [T_{\ell,\mu'}, T_{L,M}]] = \sum_{\lambda} A_{\ell L \lambda \mu \mu' M} T_{\lambda, M+\mu+\mu'}, \quad (2.6.11)$$

where the calculation of the coefficients $A_{\ell L \lambda \mu \mu' M}$ is tedious but straightforward. The last term in equation (2.6.10) can be evaluated using equation (2.6.8):

$$\begin{aligned} & \left\langle \int_0^\infty d\tau \exp(i\omega\mu t + i\omega\mu'(t-\tau)) V_{\ell,-\mu}(t) V_{\ell,-\mu'}(t-\tau) \right\rangle_{av} \\ &= \int_0^\infty d\tau \exp(i\omega\mu t + i\omega\mu'(t-\tau)) \left(\frac{1}{2\ell+1} \right) (\delta_{-\mu,\mu'}) (-1)^\mu \\ & \quad \times V_{\ell,-\mu}^2 e^{-\tau/\tau_c} \\ &= (-1)^\mu (V_{\ell,-\mu}^2 \tau_c) \left(\frac{1}{2\ell+1} \right) \left(\frac{1}{i\omega\mu\tau_c - 1} \right) \delta_{-\mu,\mu'}. \end{aligned} \quad (2.6.12)$$

The term $\delta_{-\mu,\mu}$, prevents the unphysical results discussed above.

Substituting (2.6.11) and (2.6.12) into (2.6.10), and changing the sign of the dummy index μ , yields

$$\begin{aligned} & \sum_{L,M} (-1)^M T_{L,M} \frac{d}{dt} \sigma_{L,-M} \\ &= \sum_{L,M} (-1)^M \sigma_{L,-M} \sum_{\mu,\lambda} \frac{A_{\ell L \lambda \mu - \mu M} (-1)^\mu V_{\ell \mu}^2 \tau_c}{(2\ell+1)(1+i\omega\tau_c)} T_{\lambda,M} . \end{aligned} \quad (2.6.13)$$

Equation the coefficients of T_{LM} on both sides yields

$$\frac{d}{dt} \sigma_{L,-M} = \sum_{L',\mu} \frac{A_{\ell L' L \mu - \mu M} (-1)^\mu V_{\ell \mu}^2 \tau_c}{(2\ell+1)(1+i\omega\tau_c)} \sigma_{L',-M} . \quad (2.6.14)$$

Equating (2.6.14) is identical to equations (23) and (24) of reference (8) except that V^2 is replaced by $V_{\ell \mu}^2$, which must then be brought inside the summation over μ . A few examples of equation (2.6.14), for the special case of a spin-3/2 particle, are given below.

For $\ell = 1$:*

$$\frac{d}{dt} \sigma_{10} = - \frac{2}{15} \tau_c \left(\frac{V_{11}^2}{1+(\omega\tau_c)^2} \right) \sigma_{10} \rightarrow - \frac{2}{15} \tau_c V_{11}^2 \sigma_{10} \quad (2.6.15a)$$

$$\frac{d}{dt} \sigma_{11} = - \frac{1}{15} \tau_c (V_{10}^2 + \frac{V_{11}^2}{1+(\omega\tau_c)^2}) \sigma_{11} \rightarrow - \frac{1}{15} \tau_c (V_{10}^2 + V_{11}^2) \sigma_{11} \quad (2.6.15b)$$

$$\frac{d}{dt} \sigma_{20} = - \frac{2}{5} \tau_c \left(\frac{V_{11}^2}{1+(\omega\tau_c)^2} \right) \sigma_{20} \rightarrow - \frac{2}{5} \tau_c V_{11}^2 \sigma_{20}, \text{ and} \quad (2.6.15c)$$

*the symbol " \rightarrow " indicates the limit $\omega\tau_c \ll 1$

$$\frac{d}{dt} \sigma_{21} = - \frac{1}{15} \tau_c (V_{10}^2 + \frac{5V_{11}^2}{1+(\omega\tau_c)^2}) \sigma_{21} \rightarrow - \frac{1}{15} \tau_c (V_{10}^2 + 5V_{11}^2) \sigma_{21} \quad (2.6.15d)$$

For $\ell = 2$:

$$\begin{aligned} \frac{d}{dt} \sigma_{10} &= - \frac{2}{25} \tau_c \left[\left(\frac{V_{21}^2}{1+(\omega\tau_c)^2} + \frac{4V_{22}^2}{1+(2\omega\tau_c)^2} \right) \sigma_{10} \right. \\ &\quad \left. - \frac{1}{\sqrt{3}} \left(\frac{V_{21}^2}{1+(\omega\tau_c)^2} - \frac{V_{22}^2}{1+(2\omega\tau_c)^2} \right) \sigma_{30} \right] \\ &\rightarrow - \frac{2}{25} \tau_c \left[(V_{21}^2 + 4V_{22}^2) \sigma_{10} - \frac{1}{\sqrt{3}} (V_{21}^2 - V_{22}^2) \sigma_{30} \right], \quad (2.6.16a) \end{aligned}$$

$$\begin{aligned} \frac{d}{dt} \sigma_{11} &= - \frac{1}{25} \tau_c \left[(3V_{20}^2 + \frac{5V_{21}^2}{1+(\omega\tau_c)^2} + \frac{2V_{22}^2}{1+(2\omega\tau_c)^2}) \sigma_{11} \right. \\ &\quad \left. - \sqrt{6} \tau_c (-V_{20}^2 + \frac{V_{22}^2}{1+(2\omega\tau_c)^2}) \sigma_{31} \right] \\ &\rightarrow - \frac{1}{25} \tau_c \left[(3V_{20}^2 + \text{t}V_{21}^2 + 2V_{22}^2) \sigma_{11} \right. \\ &\quad \left. + \sqrt{6} (V_{20}^2 - V_{22}^2) \sigma_{31} \right], \quad (2.6.16b) \end{aligned}$$

$$\begin{aligned} \frac{d}{dt} \sigma_{20} &= - \frac{2}{5} \tau_c \left(\frac{V_{21}^2}{1+(\omega\tau_c)^2} + \frac{V_{22}^2}{1+(2\omega\tau_c)^2} \right) \sigma_{20} \\ &\rightarrow - \frac{2}{5} \tau_c (V_{21}^2 + V_{22}^2) \sigma_{20}, \text{ and} \quad (2.6.16c) \end{aligned}$$

*the symbol " \rightarrow " indicates the limit $\omega\tau_c \ll 1$

$$\frac{d}{dt} \sigma_{21} = -\frac{1}{5} \tau_c (V_{20}^2 + \frac{V_{21}^2}{1+(\omega\tau_c)^2} + \frac{2V_{22}^2}{1+(2\omega\tau_c)^2}) \sigma_{21} \quad (2.6.16d)$$

$$\rightarrow -\frac{1}{5} \tau_c (V_{20}^2 + V_{21}^2 + 2V_{22}^2) \sigma_{21}.$$

2.6.2 Example: Electric Field Gradient

The energy operator for a particle with a total spin I and with a quadrupole moment eQ (e is the elementary charge), within a cylindrically symmetric free-space electric field with a gradient q along the field symmetry axis, is given by⁽¹⁷⁾

$$V_{op} = \frac{e^2 q Q}{4I(2I+1)} [3I_z^2 \cos^2 \theta + 3I_x^2 \sin^2 \theta + 3(I_z I_x + I_x I_z) \sin \theta \cos \theta - I^2], \quad (2.6.17)$$

where θ is the angle between the symmetry axes of the quadrupole and of the electric field, and I_z , I_x , and I^2 are spin angular momentum operators. It is easy to show that (2.6.17) is equivalent to

$$V_{op} = \frac{e^2 q Q}{4I(2I-1)} \left[\left(\frac{1}{2} (3 \cos^2 \theta - 1) \right) (3I_z^2 - I^2) + (3 \sin \theta \cos \theta) (I_z I_x + I_x I_z) + \left(\frac{1}{2} \right) (3 \sin^2 \theta) (I_x^2 - I_y^2) \right]. \quad (2.6.18)$$

Using the definition of the spherical basis operators, and defining $V_0 = e^2 q Q / 4I(2I-1)$, it can be shown that

$$V_{op} = \sum_{m=-2}^2 (-1)^m V_{2,-m} T_{2,m},$$

with

$$V_{2,0} = 6V_0 \left(\frac{1}{2}(3\cos^2\theta - 1) \right) = 6V_0 P_2(\cos\theta), \quad (2.6.19a)$$

$$V_{2,\pm 1} = \pm\sqrt{6} V_0 (3\sin\theta\cos\theta) = \pm\sqrt{6} V_0 P_2^1(\cos\theta), \text{ and} \quad (2.6.19b)$$

$$V_{2,\pm 2} = \frac{\sqrt{6}}{2} V_0 (3\sin^2\theta) = \frac{\sqrt{6}}{2} V_0 P_2^2(\cos\theta). \quad (2.6.19c)$$

The terms $P_2(\cos\theta)$ and $P_2^m(\cos\theta)$ are Legendre and associated Legendre functions. Note that V_{20} corresponds to the shift in magnetic energy levels of the spin system, and that $V_{2\pm 1}$ corresponds to a torque on the spins due to the electric field gradient.

Equations (2.6.19) are substituted into equation (2.6.16a) and (2.6.16b). Assuming that $\omega\tau_c \ll 1$ and that σ_{30} and σ_{31} are negligible compared to σ_{10} and σ_{11} , the result is

$$\frac{d}{dt} \sigma_{10} = -R_0 \tau_c V_0^2 (2 - 2\cos^2\theta) \sigma_{10}, \text{ and} \quad (2.6.20a)$$

$$\frac{d}{dt} \sigma_{11} = -R_0 \tau_c V_0^2 (1 + \cos^2\theta) \sigma_{11}, \quad (2.6.20b)$$

where the constant R_0 is equal to $54/25$, and where θ is now the angle between the electric field symmetry axis and the quantization direction. The latter is determined by the static magnetic field in magnetic resonance experiments.

Equations (2.6.20) make some strange predictions. For instance, at $\theta = 90^\circ$ they predict that the longitudinal spin distribution relaxes twice as fast as the transverse distribution. This is not in agreement with magnetic-resonance relaxation-time measurements, where the transverse

relaxation rate $1/T_2$ is always faster than or equal to the longitudinal rate $1/T_1$. However, the above calculation does not consider isotropic mechanisms which can considerably increase the actual transverse relaxation rate.

2.6.3 Wall Relaxation for Various Container Shapes

The relaxation of spins of vapor-phase atoms occurs on the wall of the container or cell⁽¹⁸⁾. Each portion of the wall makes a fixed angle with respect to the static magnetic field H_0 , and therefore the relaxation rate due to a fluctuating anisotropic quadrupole perturbation can be calculated by summing or integrating the angle-dependent relaxation rates (equations 2.6.20) over the cell surface. The electric field gradients arising from the cell wall have their symmetry axes perpendicular to the wall surface. Therefore, θ in equations (2.6.20) represents the angle between H_0 and the normal to the cell surface. For a spherical container, the relaxation rate is obviously independent of cell orientation. The variation of relaxation rate for spin-3/2 atoms due to electric field gradients on the walls versus changes in cell orientation for other shapes is summarized below (see Figures 2.6.1 and 2.6.2).

Cube-Shaped Cell:

When the cube is oriented with its faces parallel or perpendicular to H_0 , there are four faces parallel to H_0 ($\theta = 90^\circ$) and two faces perpendicular ($\theta = 0$) (Figure 2.6.1, $\beta = 0^\circ$). Therefore,

$$\frac{1}{\sigma_{10}} \frac{d}{dt} \sigma_{10} = -R_0 \tau_c V_0^2 [4(2) + 2(0)] = -8 R_0 \tau_c V_0^2, \text{ and} \quad (2.6.21)$$

$$\frac{1}{\sigma_{11}} \frac{d}{dt} \sigma_{11} = -R_0 \tau_c V_0^2 [4(1) + 2(2)] = -8 R_0 \tau_c V_0^2.$$

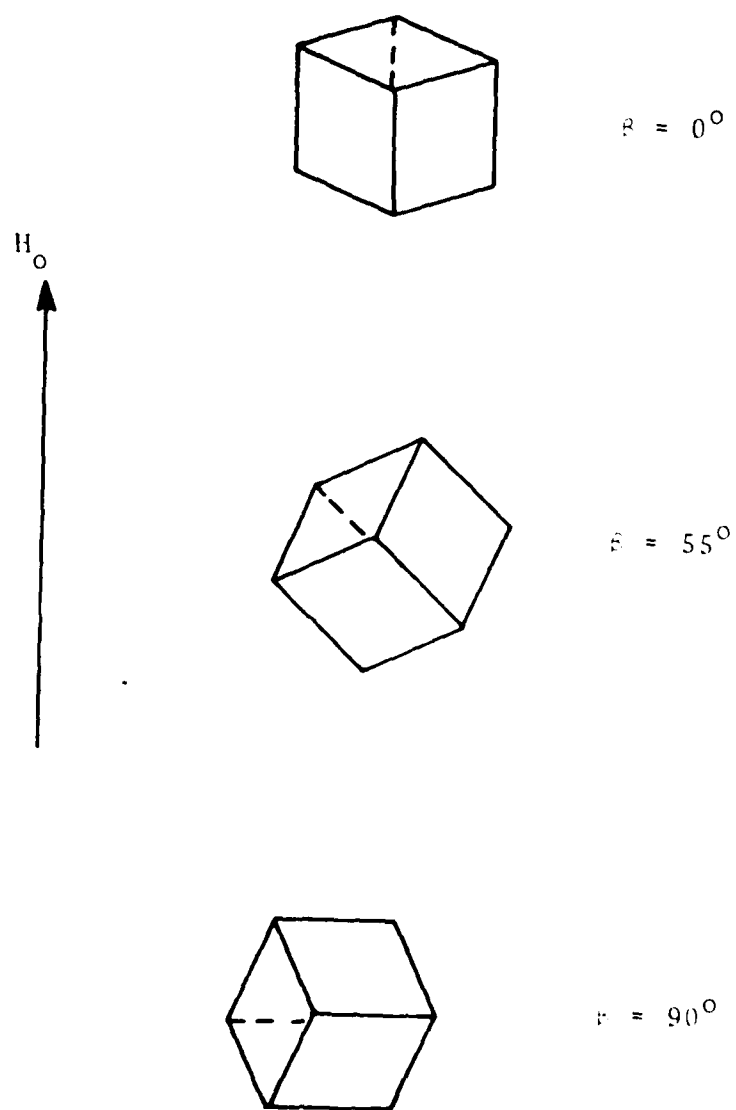


FIGURE 2.6.1 - Orientation for Cube-Shaped Cell

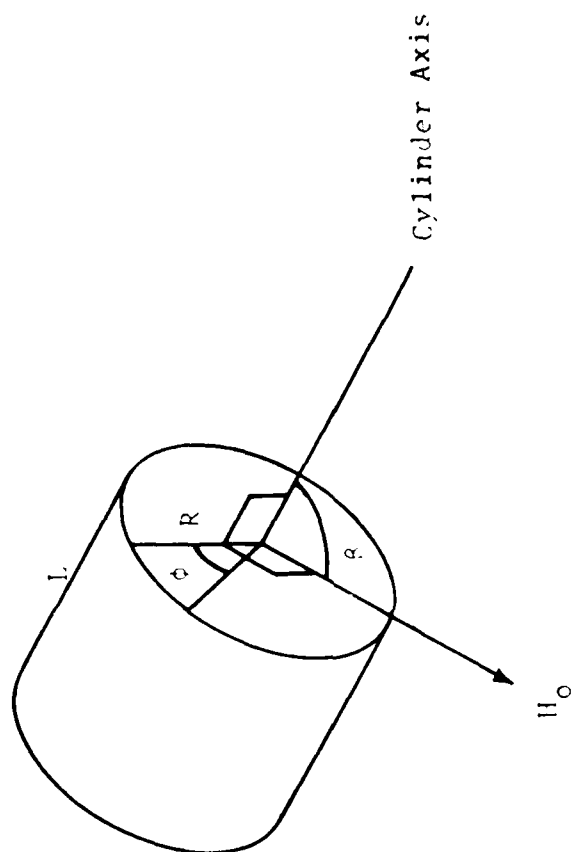


FIGURE 2.6.2 - Cylindrical Cell

When the cube is oriented with H_0 along a body diagonal, it can be shown that the normals to all cube faces make an angle of 54.74° with H_0 (Figure 2.6.1, $\beta = 55^\circ$). This is the angle for which V_{20} , the shift in energy levels, is zero. Then

$$\frac{1}{\sigma_{10}} \frac{d}{dt} \sigma_{10} = -R_0 \tau_c V_0^2 [6(4/3)] = -8 R_0 \tau_c V_0^2, \text{ and}$$

$$\frac{1}{\sigma_{11}} \frac{d}{dt} \sigma_{11} = -R_0 \tau_c V_0^2 [6(4/3)] = -8 R_0 \tau_c V_0^2. \quad (2.6.22)$$

When the cube is oriented so that two sides are parallel to H_0 and four sides make an angle of 45° , (Figure 2.6.1, $\beta = 90^\circ$),

$$\frac{1}{\sigma_{10}} \frac{d}{dt} \sigma_{10} = -R_0 \tau_c V_0^2 [2(2)+4(1)] = -8 R_0 \tau_c V_0^2, \text{ and} \quad (2.6.23)$$

$$\frac{1}{\sigma_{11}} \frac{d}{dt} \sigma_{11} = -R_0 \tau_c V_0^2 [2(1)+4(3/2)] = -8 R_0 \tau_c V_0^2.$$

It can be shown that for all cube orientations in which a face diagonal (dotted line in Figure 2.6.1) is perpendicular to H_0 , the relaxation rates for σ_{10} and σ_{11} are equal and are independent of cube orientation. This is not in agreement with previous predictions⁽¹⁹⁾. However those calculations did not include the $T_{2,+1}$ and $T_{2,+2}$ terms.

Right-Circular Cylinder:

Consider a closed right circular cylinder with radius R and length L , define $\epsilon = L/R$, and let β be the angle between H_0 and the cylinder axis. On the end faces, the angle θ between H_0 and the surface normal is equal to β , while for points on the curved

surface, this angle is given by $\cos\theta = \sin\theta\sin\beta$, where the azimuthal angle ϕ is shown in Figure 2.6.2. Integrating over the entire surface,

$$\frac{d}{dt} \sigma_{10} = -R_o \tau_c V_o^2 (4\pi R^2) (1 + \epsilon - \frac{\epsilon}{2} \sin^2\beta - \cos^2\beta) \sigma_{10}, \text{ and}$$

$$\frac{d}{dt} \sigma_{11} = -R_o \tau_c V_o^2 (2\pi R^2) (1 + \epsilon + \frac{\epsilon}{2} \sin^2\beta + \cos^2\beta) \sigma_{11}. \quad (2.6.24)$$

For a long cylinder ($\epsilon \gg 1$), this reduces to

$$\frac{d}{dt} \sigma_{10} = -R_o \tau_c V_o^2 (4\pi R^2 \epsilon) (1 - \frac{1}{2} \sin^2\beta) \sigma_{10}, \text{ and}$$

$$\frac{d}{dt} \sigma_{11} = -R_o \tau_c V_o^2 (2\pi R^2 \epsilon) (1 + \frac{1}{2} \sin^2\beta) \sigma_{11}. \quad (2.6.25)$$

while for a flat disk ($\epsilon \ll 1$)

$$\frac{d}{dt} \sigma_{10} = -R_o \tau_c V_o^2 (4\pi R^2) (1 - \cos^2\beta + \epsilon (1 - \frac{1}{2} \sin^2\beta)) \sigma_{10}, \text{ and}$$

$$\frac{d}{dt} \sigma_{11} = -R_o \tau_c V_o^2 (2\pi R^2) (1 + \cos^2\beta) \sigma_{11}. \quad (2.6.26)$$

Note that the longitudinal and transverse relaxation rates become equal to each other at $\beta = 54.74^\circ$ for any value of ϵ . Again, this is the angle for which V_{20} , the shift in the energy levels, is zero.

These relaxation rates do vary with cell orientation. At $\beta = 0$

for the cylinder and $\beta = 90^\circ$ for the disk, the longitudinal relaxation rate is twice the transverse rate. Again note that these rates are due only to the anisotropic quadrupole perturbation, and not to other effects such as dipole perturbations.

2.6.4 Experimental

Measurements of longitudinal and transverse relaxation rates were made using a cube-shaped cell. The fused-silica cube, approximately 1 cm on a side, was evacuated and then filled with a dry vapor of mercury enriched with the isotopes ^{199}Hg and ^{201}Hg at a density of about 10^{12} atoms/cm³. The cell did not contain a buffer gas.

The transverse orientation moment was detected by means of the transverse rf Faraday effect using the apparatus described in Section 1.2. Relaxation rates were determined using modified pulsed NMR techniques.⁽²⁰⁾ At the start of each measurement, both shutters were closed, and no current was applied to the AC coils. A longitudinal moment was established by opening the pump-beam shutter for 60 seconds, which is about ten times longer than the pumping time. The pumping time is the time required to orient a fraction $1/e$ of the atoms, assuming no relaxation. For measurement of the longitudinal relaxation rate $1/T_1$, the pump shutter was closed, and, after a measured delay, the readout shutter was opened simultaneously with the application of a short pulse through the AC coils. This pulse was controlled by the switching circuit and was adjusted such that the longitudinal moment was rotated by 90° , making it observable with Faraday readout. The resulting amplitude was recorded on a T-Y recorder for various values of the delay time. The amplitude (after the pulse) versus the delay time can be least-squares fitted to an exponential function to determine the relaxation rate. For measurement of the transverse relaxation rate $1/T_2$, the pulse was applied simultaneously with the closing of the pump-beam shutter, so that a transverse distribution existed during the measured delay time, after which the readout shutter

was opened and the signal was observed. Note that the readout and pump light could not affect the measured relaxation rates, since all relaxation took place with both beams off.

It is important to check for the presence of non-exponential decay when analyzing the results of this experiment^(1,5). Such departure from exponential decay can occur if V_{20} , the shift in the magnetic energy levels due to the quadrupole perturbation, does not average to zero over the entire cell surface (see Section 2.4). It can be shown that this average, $\langle V_{20} \rangle$, is zero over the surface of a cube for all orientations with respect to the H_0 magnetic field. A nonzero average can be caused by the presence of the cell sealoff tip (a major source of this effect in spherical cells) or by a slight elongation of the cell shape (the cell walls were not flat enough to verify any elongation). It can be shown that either of these two effects will result in a value of $\langle V_{20} \rangle$ which has the same angular dependence as V_{20} itself:

$$\langle V_{20} \rangle \propto P_2(\cos\theta) = \frac{1}{2}(3\cos^2\theta - 1), \quad (2.6.27)$$

where θ is now the angle between H_0 and an axis whose orientation with respect to the cell depends upon the cell shape. The functional form of the decay transient for transverse relaxation is shown in Section 2.4 to be given by

$$S(t) = S(0)e^{-t/\tau} (2 + 3\cos\omega_Q t) \quad (2.6.28)$$

where $S(t)$ is the signal at time t , τ is the relaxation time, and $S(0)$ is proportional to $\langle V_{20} \rangle$. Longitudinal decay transients are believed to be unaffected by a nonzero $\langle V_{20} \rangle$.

Measurements of longitudinal and transverse relaxation rates, $1/T_1$ and $1/T_2$, were made for a cube-shaped cell in several orientations. Specifically, measurements were made along the three equivalent $\theta = 0^\circ$ axes, three

of the four equivalent $\beta = 55^\circ$ axes, and three of the six equivalent $\beta = 90^\circ$ axes. The axes are identified by numbers in Figure 2.6.3. The term "equivalent axes" refers to the fact that a given value of β can be obtained with respect to different cube faces. For instance, the $\beta = 55^\circ$ axis can be obtained by aligning H_0 along any of the four cube body diagonals. The individual cube faces can be identified by features such as bubbles, scratches, or the location of the sealoff tip (not shown in Figure 2.6.3).

Longitudinal and transverse decay transients were nonlinear-least-squares fitted to equation (2.6.28). All of the longitudinal decay transients yielded ω_Q equal to zero, within experimental uncertainty, and relaxation times between 40 and 44 seconds, showing no apparent variation with cell orientation. The transverse decay transients yielded relaxation times a few percent shorter than the corresponding longitudinal relaxation times, and values of ω_Q as shown in Table 2.6.1.

Note that the values of ω_Q are roughly proportional to $[P_2(\cos\theta)]$. Therefore, if the cell is assumed to be elongated along axis #3 in Figure 2.6.3, then the results can be explained in terms of the non-exponential decay which is predicted for cells with such a shape.

Previous results⁽¹⁹⁾ had indicated that the transverse relaxation rate did vary with the cube orientation. It is now believed that the apparent variation was due to a small departure from exponential decay, which was not severe enough to cause a noticeable curvature in a logarithmic plot of signal vs time (which should be a straight line for an exponential decay), but was able to affect the apparent slope of the line, which is proportional to the relaxation rate. The previous experiments were not conducted on more than one of the equivalent cube axes, and they did not measure longitudinal relaxation rates.

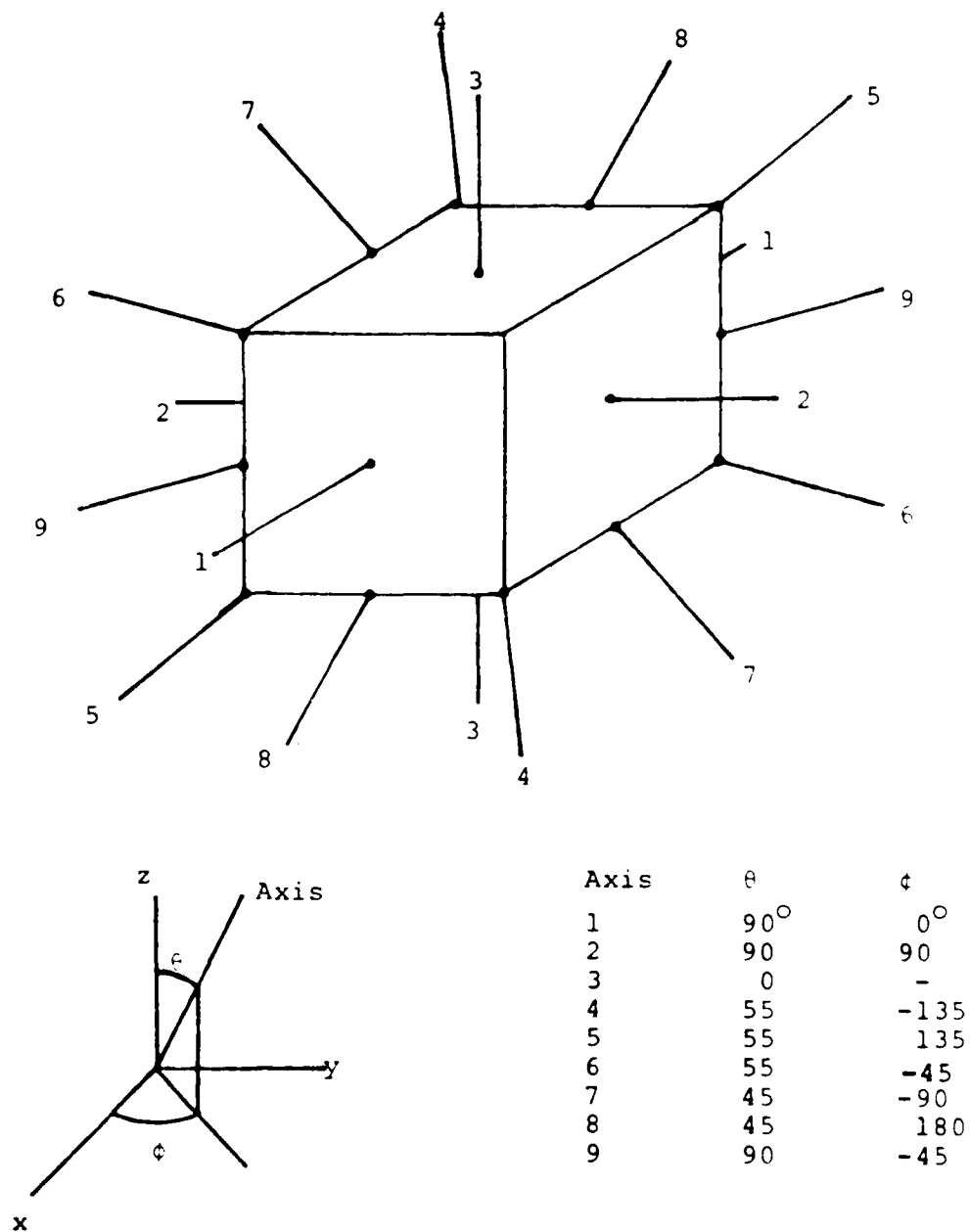


FIGURE 2.6.3 - Axes of Orientation of Magnetic Field
With Respect to Cube-Shaped Cell

THE SINGER COMPANY • KEARFOTT DIVISION

TABLE 2.6.1 - Values of Quadrupole-Splitting Parameter
for Various Cube-Shaped Cell Orientations

Axis #	θ (see Figure 4)	$\omega_Q (x10^3)$ (Hz)	$P_2 (\cos\theta)$
1	0	$8.3 \pm 1.5^*$	-0.5
2	0	14.3 ± 1.3	-0.5
3	0	21.5 ± 0.8	1
4	55	$5.1 \pm 2.6^*$	0
5	55	0.0 ± 0.1	0
6	55	0.0 ± 0.1	0
7	90	5.1 ± 1.9	.15
8	90	6.4 ± 3.1	.25
9	90	10.1 ± 1.6	-0.5

*values not reproducible from day to day

2.7 CONCLUSIONS

The results described in this section show that the four-level spin system of ^{201}Hg can be conveniently described in terms of spherical basis operators, and that this description can predict effects which are not predicted by the simpler but less rigorous description of ^{201}Hg as three two-level spin systems. The results also indicate that a description of a quadrupole perturbation solely in terms of the shift in energy levels, without including the effects of torques which may also be present, might not be sufficient for predicting the effects of such a perturbation.

3. CELL FABRICATION AND TESTING

3.1 TIP-ONLY HEAT TREATMENTS

The surface of the cell near the sealoff tip can be expected to be different from the remainder of the cell surface, since the latter is baked for several days to achieve maximum cleanliness while the former is freshly created, by glassblowing, at the time of sealoff, and is never subsequently baked in a high-vacuum system. It had been suggested that only this unbaked surface near the cell tip is responsible for the strong relaxation observed in cells just after sealoff, and that the changes in the cell surface which are caused by heat treatments occur mostly at that area. This hypothesis was tested by applying heat treatment only to the tip area.

Two cells, C-2 and W-165, were given tip-only heat treatments to determine if the cell tip area is the dominant region of the cell surface for mercury relaxation. The first treatment was done in a small funnel-shaped apparatus made from fused silica, sketched in Figure 3.1.1a. After a one-hour heat treatment at 920°C , neither cell showed signals. However, a thermocouple placed inside the tip of a dummy cell (Figure 3.1.1b) showed that the temperature inside the tip probably had not exceeded 500°C . It was found that three turns of nichrome wire, placed directly around the cell tip, could raise the inside temperature to about 750°C , as measured by the thermocouple. In the past, most cells showed moderate signals after a 750°C heat treatment, but these two cells still showed no signals after a second tip-only heat treatment with the heater wire directly on the cell tip as described above. The cells were then given a one-hour heat treatment in an oven at 750°C after which they showed moderate signals but short ($<2\text{s}$) relaxation times. These results strongly suggest that the relaxation of the nuclear spins is not confined to the tip area, but that it occurs over the entire inner surface of the cell.

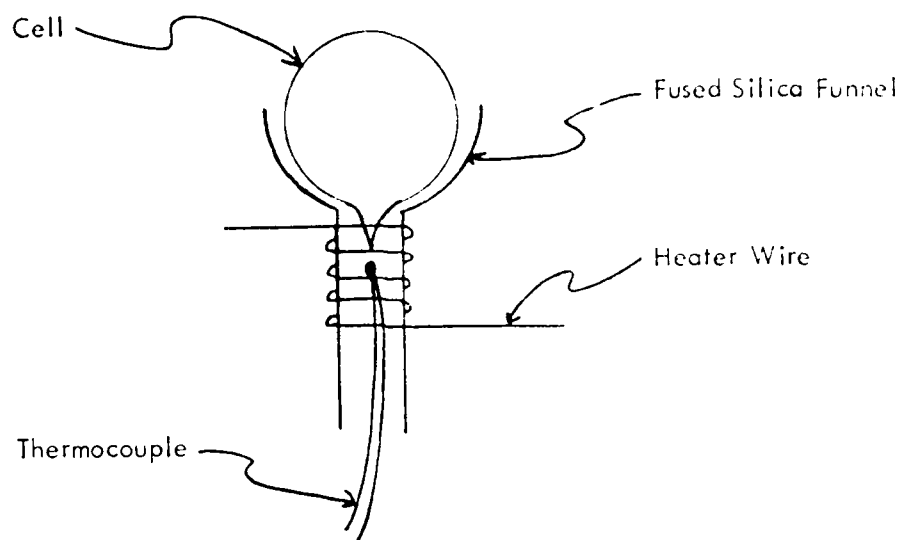


FIGURE 3.1.1a - Cell Tip-Only Heater

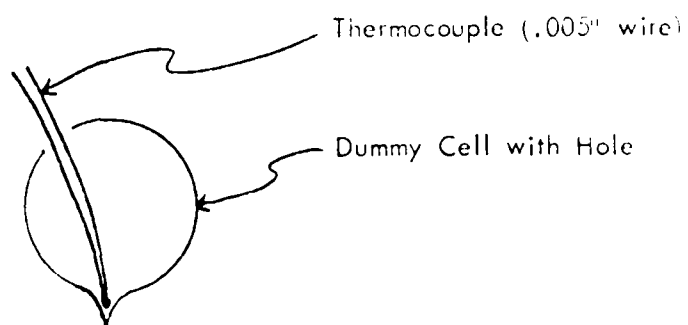


FIGURE 3.1.1b - Thermocouple Inside Cell Tip

The two cells then were given a 930°C, one-hour heat treatment. Cell W-165 then showed maximum relaxation times of 70s for ^{199}Hg (at 150°C) and 56 s for ^{201}Hg (at 300°C). These values are similar to those of other cells made from the same material. Cell C-2 showed performance slightly poorer than that of W-165. Both cells improved after the 930°C heat treatment, but not after the tip-only heat treatment, which further indicated that the mercury relaxation is affected by changes which occur over the entire cell surface.

3.2 EFFECTS OF ABBREVIATED HEAT TREATMENT PROCEDURE

Nearly all of the cells made during the past few years were given a series of one-hour heat treatments at about 750°C, 850°C, and 925°C. Signal strengths and relaxation times usually increased after each heat treatment, and rarely improved significantly after additional heat treatments. A test was conducted to determine whether the first two heat treatments were necessary for achieving good cell performance. Five cells from the same batch were used for this test. Two of them received the sequence of three heat treatments at different temperatures, and the other three received heat treatments only at the highest temperature. The relaxation times of these cells at 200°C are shown in Table 3.2.1 below. These results indicate that the 765°C and 860°C treatments are not crucial and that the 930°C heat treatment is the most effective toward improving cell performance. The first two heat treatments have therefore been omitted during processing of cells made after this test.

TABLE 3.2.1 - τ_{199}/τ_{201} at 200°C After Different Heat Treatment Sequences

Cell Treatment	W-156 High Temperature	W-159 High Temperature	W-162 Only	W-157 Standard	W-160 Standard
After 765°C	-	-	-	0.6/1.4	0.8/1.6
After 860°C	-	-	-	72/34	70/33
After 930°C	53/27	96/32	14/19	70/29	85/30
After 930°C	70/29	86/29	42/19	69/28	74/27

3.3 THE CAGNAC CELL STABILIZATION METHOD

A heat treatment procedure was suggested by B. Cagnac⁽²¹⁾, who was able to produce stable cells by repeatedly cycling the cell temperature between room temperature and 400°C while continuously exposing the cells to resonant ultraviolet radiation. This procedure was tested recently, using cells prepared on both ion pumped and oil-diffusion pumped vacuum systems.

Three cells from the batch used to test the abbreviated heat treatment (see Section 3.2 above) received the Cagnac treatment. The first four heat cycles were done in the relaxation-time measurement apparatus. The relaxation times were short, but the cells improved slightly with each cycle. For instance, typical ²⁰¹Hg relaxation times at 400°C were 0.9 s, 1.2 s, 1.5 s, and 2.0 s during the four respective heat cycles. Next, the cells received 26 heat cycles in a different oven, exposed to strong resonant uv, which caused a slight decrease in relaxation time, but a drastic decrease in mercury vapor density. At this point, the observed relaxation times were not more than a few seconds. Finally, the cells were given a 930°C heat treatment, after which their vapor densities and relaxation times were comparable to the other cells in the batch after a 930°C heat treatment. Typical relaxation times at this point are shown in Table 3.3.1, and can be compared with values for other cells from the same batch shown in Table 3.2.1. Subsequent exposure to strong resonant uv caused the relaxation times to drop to as low as one tenth of the values shown in Table 3.3.1, as well as causing a slight reduction in vapor density. The results on these cells do not duplicate Dr. Cagnac's results. The monotonic increase in relaxation time with temperature and gradual overall increase in relaxation time with successive heat cycles which were observed with these cells, are not observed in the cells prepared using the usual methods. Most cells exhibit long relaxation times only after high-temperature heat treatment, rather than after low-temperature heat cycling with resonant uv.

TABLE 3.3.1 - Relaxation Times after Cagnac Cycles followed by a 930° Heat Treatment

Cell	$\tau_{199}(200^{\circ}\text{C})$	$\tau_{201}(200^{\circ}\text{C})$
W-155	55	32
W-158	78	34
W-161	63	27

A new batch of cells was then fabricated and filled using the oil-diffusion-pump vacuum system in order to duplicate more closely the experimental method used by Cagnac. The cells were baked at 1000°C for two days, but a leak became evident when the cells were cooled. Fortunately, the leak was found before the mercury ampoule had been broken. The leak was fixed and the cells were baked again for several days at 1000°C with the system pressure going as low as 2×10^{-8} torr with all heaters on. The cells were cooled slowly to 700°C and the oven was then removed. The mercury ampoule was cooled to about 0°C, and, when the break-tip seal was broken, the system pressure gradually rose to about 5×10^{-7} torr. At this point, a glass valve was closed, isolating the cells and ampoule from the rest of the system. The mercury was driven into the cell manifold, which was then sealed off from the vacuum system. The cells were kept at elevated temperatures with the manifold tip in liquid nitrogen for four days, after which the cells were removed from the manifold.

The batch was divided into two groups of four cells each. The control group received heat treatments at 940°C and at 950°C for one hour, and the test group received 29 heat cycles exposed to resonant uv. NMR signals were sought during the first three heat cycles and during the last heat cycle, but no signals were found. This group of cells was then given a 940°C one hour heat treatment, after which strong signals were observed. The results for all cells are summarized in Table 3.3.2 below. Note that there is no significant difference between the performances

of cells from the two groups after the first heat treatment, and that the performance of the control group degraded slightly after the second heat treatment. Excessive heat treatments have been observed to degrade the performance of cells in previous batches.

TABLE 3.3.2 - Relaxation Times for Cells Prepared on Oil-Diffusion Pump System

Group	Cell	After First Heat Treatment				After Second Heat Treatment			
		200°C		Maximum		200°C		Maximum	
		199	201	199	201	199	201	199	201
Test	W-167	78 s	36 s	78 s	52 s	-	-	-	-
	W-169	94	39	94	44	-	-	-	-
	W-171	109	45	109	61	-	-	-	-
	W-173	83	43	108	62	-	-	-	-
Control	W-168	90 s	39 s	98 s	55 s	75 s	34 s	75 s	46 s
	W-170	91	33	91	53	74	29	74	39
	W-172	129	44	129	69	113	41	113	61
	W-174	119	45	119	63	120	43	120	62

Although the current batch of cells was filled using an oil diffusion pumped vacuum system, similar to the system used by Cagnac, his results were still not reproduced here, since no signals were observed before the 940°C heat treatment.

5.4 WATER-FREE SPECTROSIL CELLS

A water-free form of the Spectrosil brand of fused silica (Thermal-American Fused Quartz Co., Montville, NJ) has recently become available. The suitability of this type of silica for cell fabrication was tested by making a batch of four cells (C-1 through C-4) from this material and four cells (W-163 through W-166) made from Suprasil W, the material normally

used for cells. In a new cell bakeout technique, applied for the first time to this batch, the high temperature cell bakeout was not started until the vacuum system pressure had dropped to 10^{-8} torr with the entire system at 400°C . The pressure rose more than expected when the cells and manifold of this batch were first heated to 1000°C , but it then decreased as cell bakeout was continued.

Cells W-165 and C-2 received the tip-only heat treatments described in Section 3.1. The other six cells received 930°C heat treatment for one hour. The performance of these cells is summarized in Table 3.4.1 below.

TABLE 3.4.1 - Water-free Spectrosil/Suprasil Cells
After One Heat Treatment

Cell	200°C	τ_{199} , sec		200°C	τ_{201} , sec	
		250°C	Maximum		250°C	Maximum
C-1	5	33	59	16	42	63
C-3	15	36	70	19	40	63
C-4	6	35	65	14	38	53
W-163	102	-	102	44	-	68
W-164	91	107	107	42	56	64
W-166	76	98	43	59	59	67
C-3*	13	50	86	17	41	58
C-4*	3	17	23	10	30	40

*after second heat treatment

The relaxation times of the water-free Spectrosil cells did not rise as quickly with temperature as those of the cells made from Suprasil W, and their maximum values were not as high. Therefore, the three Spectrosil cells were given another heat treatment, at 945°C for one hour. Cell C-1 lost most of its mercury vapor, and cells C-3 and C-4 showed slightly poorer overall performance. These results indicate that water-free

Spectrosil is not as good a starting material as Suprasil W.

3.5 MERCURY PURIFICATION

During the reporting period, many techniques were developed for improving the purity of mercury and for handling it under vacuum. Most of these techniques were developed during fabrication of the electrodeless lamps which are needed for these optical pumping experiments, and therefore, the effects of such techniques upon relaxation in NMR cells have not yet been determined.

The isotopically-enriched mercury is currently being received in the form of mercury oxide, and not in the form of mercury metal as had been received previously. The oxide is reduced by heating under vacuum. During such heating, oxygen is released, along with smaller quantities of water and other atmospheric constituents. A residue remains after the mercury has been distilled away from the area where the oxide is decomposed. Efforts are currently underway to identify this residue.

The mercury then receives multiple distillations under vacuum, using a long vertical silica tube and a movable ring-shaped cold trap. The mercury droplet is placed at the closed bottom end of the tube and the top end of the tube is attached to the vacuum system. The ring-shaped cold trap is placed around the tube, about two inches above the mercury. When the mercury is heated, it evaporates and then condenses as a thin film near the cold trap. The trap is then raised two inches and the process is repeated. In this manner, the mercury can get distilled several times without having to be driven for long distances within the vacuum system.

Once the reduction and distillation has been completed, the purified mercury is isolated in a break-tip ampoule during the high-temperature bakeout of the cells or lamps. Therefore, any impurities generated during bakeout cannot come in contact with the purified mercury. The use of

such ampoules is probably the most important step in maintaining the mercury purity, since mercury is excellent getter and will readily absorb many contaminants.

When the break-tip seal is opened, a small but significant "puff" of gas can be detected by the residual gas analyzer. This indicates that some outgassing has occurred inside the sealed-off ampoule. To reduce the effects of such outgassing, a non-evaporable getter (S.A.E.S. ST-171) was placed in a side-arm attached to one of the ampoules, in order to absorb any outgassed impurities. The getter can act as a pump only after it is activated by heating to about 900°C. Unfortunately, a large amount of organic impurities was released during the activation, and it took several days to reduce the concentration of these impurities to an acceptable level. The ampoule containing the getter and the multiple-distilled mercury was then sealed off. When it was opened several days later, no puff of gas was detected. However, the organic impurities again showed up as the mercury was heated to be driven into the lamps. Therefore, more work is needed in order to utilize the getters most effectively, although they do show promise for improving the mercury cleanliness.

As mentioned above, these techniques were developed mostly while fabricating lamps. In the near future, they will be used for filling NMR cells, and their effects upon cell performance will then be tested.

4. COMPLEMENTARY INVESTIGATIONS

4.1 SURFACE ANALYSIS OF CELL WALL MATERIALS

In the past, much information on the relaxation of mercury nuclear spins has been obtained through measurements of the decay rate of signals arising from optically-detected precession of the spins. However, this technique cannot measure directly the interaction between the cell wall and a mercury atom at a specific site on the wall during a single short sticking time, and it cannot characterize the state of the wall surface, except in general macroscopic terms. Various surface spectroscopic techniques, including X-ray photoelectron spectroscopy (XPS or ESCA), secondary-ion mass spectroscopy, ion scattering spectroscopy, and Auger electron spectroscopy, recently have become readily available. These techniques are sensitive to the atomic composition and oxidation states of the atoms in the first few atomic layers, which is the portion of the cell which interacts most strongly with the nuclear spins of the mercury vapor atoms. X-ray photoelectron spectroscopy can identify the atoms present at the surface and can also determine their oxidation state. Secondary-ion mass spectrometry is extremely sensitive for detection of certain impurities, especially alkali metal atoms. Ion scattering spectroscopy is sensitive only to the outermost atoms at the surface, which are the atoms which interact most strongly with the mercury nuclear spins. Auger electron spectroscopy is sensitive to the electronic state of the surface atoms, and has an imaging capability with a resolution of 0.2 microns.

The main disadvantage of these techniques is that the cell must be broken in order to perform the analyses. It is possible that the cell wall might change during the process of breaking the cell, mounting a piece of the cell wall into a sample holder, and inserting it into the vacuum system for analysis. Despite this drawback, these analysis techniques can aid greatly in characterizing the impurities present on the cell surface.

Several cell surfaces were analyzed by XPS. This technique was chosen because knowledge of the oxidation state of the atoms was desirable and because XPS causes the least amount of damage to surfaces such as silica. The analyses were performed at the analytical laboratory of Perkin-Elmer, Physical Electronics Div., Eden Prairie, Minn.

Three cells were investigated: W-133 (a high-quality cell), W-132 (a high-quality cell which had been degraded by exposure to resonant uv) and a control cell (a cell which had been sealed off with mercury, but had not been heat treated). All cell surfaces were found to have silicon and oxygen in chemical states identical to that of SiO_2 . No mercury and no other impurities were detected. No differences in surface composition or structure were found, except for variations in the distribution of chemical states of carbon adsorbed from the lab atmosphere. It is not known whether this difference was significant in relation to cell performance or if it was due to random variations among the samples. The results of these tests indicate that the difference between good and bad cells is not due to an overall change in composition, but that it is due either to some subtle change of the entire cell surface or to a gross change of a small portion of the cell surface area. The sealoff tip was considered to be a likely area for such a gross change (see Section 3.1).

These observations indicate that the fabrication, bakeout, and processing of the cells remove most foreign substances and result in cells with clean SiO_2 walls. Hydrogen, as well as oxygen combined with elements other than silicon, may also have been present, but could not be observed by the techniques employed.

1.2 SILICA GLASSBLOWER'S SMOKE

It had been suggested that the relaxation of mercury in fused silica cells might be affected by particles of so-called "glassblower's smoke" which may end up in the cell after sealoff. This "smoke" is a white, powdery film which is produced during the strong heating needed for shaping of

fused silica or for sealoff of cells. Although some sources claim that it is composed of silicon monoxide (SiO) it was determined by XPS surface analysis to be fused silica (SiO_2). However, such small particles of fused silica may have different surface properties than the silica of the cell wall, and may cause relaxation of the mercury nuclear spins. Experiments were performed to test whether such smoke would be affected by the heat treatments which are known to improve the performance of NMR cells.

Several samples of silica "glassblower's smoke" were prepared to test whether such smoke is affected by a typical 950°C cell heat treatment. The samples were divided into three groups: one receiving a bakeout at 980°C for ten days under vacuum, another receiving a similar baking in the ambient air, and a control receiving no treatment. After treatment, no differences among the samples were seen under a 30X microscope. The samples were then examined under an electron microscope, where again no differences could be detected. Therefore, the glassblower's smoke, if present in the cell after sealoff, is probably not eliminated by heat treatment.

A fortunate accident confirmed that glassblower's smoke is not a strong relaxation site for mercury. One of the cells, W-164 contained a clearly visible amount of glassblower's smoke on its inside surface. As can be seen from Table 3.4.1, its performance was not markedly different from that of the other Suprasil cells in this batch. Therefore, it is doubtful that the presence of small amounts of glassblower's smoke in a cell will affect its performance.

4.5 CORRELATION TIME OF THE WALL POTENTIAL DUE TO MOTION OF THE MERCURY ATOM

During attempts to explain the apparent dependence of relaxation time upon cubic cell orientation, the possibility of a long correlation time τ_c was considered. The predicted relaxation time is independent of cell

orientation only if $\omega\tau_c$ is small compared to unity, where ω is 2π times the Larmor frequency. (see Section 2.6). If $\omega\tau_c$ is not small, then both the longitudinal and transverse relaxation times should show a variation on the order of $(\omega\tau_c)^2$.

The original calculation (see Section 2.6.1) assumed that the relaxing potential was a continuous stationary random fluctuation with an exponential correlation function

$$\langle V(t)V(t + \tau) \rangle = e^{-\tau/\tau_c}. \quad (4.3.1)$$

However, a vapor-phase atom only is affected by the relaxing potential while the atom is adsorbed on the wall. The potential can be modelled as a continuous potential which is turned on when the atom is adsorbed and is turned off when the atom leaves the surface. The correlation function for this potential will be different from equation (4.3.1).

We assume that the probability of an atom remaining on the surface for a time τ is $e^{-\tau/\tau_s}$, independent of how much time the atom has already spent on the surface. Note that the average time for an atom to remain on the surface is then equal to τ_s . We also assume that the average travel time between sticking events is τ_v , so that the probability of an atom being on the surface is $\tau_s/(\tau_s + \tau_v)$. Finally, and most important, we assume that the potential during one sticking event is completely uncorrelated from the potential during another sticking event. Therefore, if τ is long enough so that a desorption and subsequent readsorption occurs between time t and time $t + \tau$, then $\langle V(t)V(t + \tau) \rangle$ must be zero.

The correlation function is the ensemble average of the product $V(t)V(t + \tau)$. This is given by

$$\begin{aligned} \langle V(t)V(t + \tau) \rangle = & \text{Prob}(\text{particle on surface at time } t) \quad (4.3.2) \\ & \times \text{Prob}(\text{particle still on surface at time } t + \tau) \\ & \quad (\text{no desorption}) \\ & \times \langle V(t)V(t + \tau) \rangle \text{ for particle remaining on surface} \end{aligned}$$

$$\begin{aligned}
 &= \left(\frac{\tau_s}{\tau_s + \tau_v} \right) (e^{-\tau/\tau_s}) (e^{-\tau/\tau_c}) \\
 &= \frac{\tau_s}{\tau_s + \tau_v} e^{-\left(\frac{1}{\tau_c} + \frac{1}{\tau_s} \right) \tau},
 \end{aligned}$$

or

$$\langle V(t)V(t + \tau) \rangle = \frac{\tau_s}{\tau_s + \tau_v} e^{-\tau/\tau_{\text{eff}}}, \quad (4.5.5)$$

with

$$\frac{1}{\tau_{\text{eff}}} = \frac{1}{\tau_c} + \frac{1}{\tau_s}.$$

Usually, τ_c is much shorter than τ_s , so $1/\tau_s$ can be neglected.

The overall effects of turning the potential on and off therefore are:

- 1) the average potential is reduced by a factor $\tau_s/(\tau_s + \tau_v)$, and
- 2) there is an upper limit of τ_s for the effective correlation time τ_{eff} of the potential.

In the special case of the cubic cell, we can not assume that different sticking events are uncorrelated. If we assume that the atom is most likely to desorb in a direction perpendicular to the surface, then the atom is most likely to end up on the opposite cube face, where the values of the quadrupole perturbation are the same. Therefore, the potentials at two successive sticking events are correlated.

The above situation was simulated using a Monte-Carlo calculation. The potential was set equal to +2 (arbitrary units) on two opposite cube faces, and to -1 on the other four faces. This corresponds to axes 1-3 in Figure 2.6.3. A particle was placed randomly on the inner surface,

and then was desorbed, with the probability of desorbing at an angle θ (relative to the normal to the surface) assumed to be proportional to $\cos\theta$.⁽²²⁾ The potential at the point where the particle hit the cube was then determined. The product of the starting and ending potentials was computed and was then averaged for 5000 random paths. The result of the calculation was that

$$\langle V(0)^2 \rangle = 2$$

$$\langle V(0)V(1) \rangle = 0.2 \quad (4.5.4)$$

$$\langle V(0)V(2) \rangle \approx 0$$

where $V(0)$, $V(1)$, and $V(2)$ are, respectively, the values of the potential at the beginning, after one trip, and after two trips across the cell. We can define a correlation time for this process in terms of the rate of decrease of $\langle V(t)V(t + \tau) \rangle$, neglecting the fact that this model only evaluates $V(t + \tau)$ for values of τ corresponding to an integral number of trips across the cell. The value of $\langle V(t)V(t + \tau) \rangle$ decreases by a factor of ten after one trip, and therefore the correlation time is roughly one half of the average travel time, since $e^{-2} \approx 1/10$. Since the actual travel times are not all equal, the degree of correlation after a time τ will be less, which means that half the average travel time is an upper limit for the effective correlation time. In the cube-shaped cell, the average travel time is approximately 10^{-4} sec, and $(\omega\tau_c)^2$ then works out to be less than 5%. Any change in relaxation times caused by this effect would be less than the uncertainty of the experimental results.

4.4 AVERAGE TRAVEL DISTANCE OF A MERCURY ATOM WITHIN A CELL

The average path length of a mercury atom across the cell was computed for spherical and cubic cells. If all angles of desorption are equally likely, then the average path length is $.667D$ for a spherical cell of diameter D , and $.925L$ for a cube with side L . If the probability for desorption at an angle θ is assumed to be proportional to $\cos\theta$,⁽²²⁾ then the average path lengths are $.75D$ and $.955L$. A cubic cell has an average path length 27% greater than a spherical cell which fits inside the cube, ($D = L$) but 27% less than a spherical cell which fits around the cube ($D = L\sqrt{3}$ = cube body diagonal). Since the relaxation time is expected to be directly proportional to the average path length, these results indicate that neither of these shapes is inherently better for achieving long relaxation times by providing a long average path, and that the best cell shape for maximizing the path length is the one that best fills the available space.

4.5 THE DARK FILM IN MERCURY LAMPS

An rf-excited electrodeless-discharge mercury lamp is a system where mercury-silica interactions are expected to be stronger than the interactions in NMR cells. The dark film which often forms in these lamps has been investigated, in order to gain insight into the mercury-silica interactions which can occur in both lamps and cells. Some of the results were described in the previous interim report⁽¹²⁾. Examination by electron microscopy had shown a complicated surface structure, and X-ray analysis (EDAX) had detected only mercury and silicon. The film was stable in acids known to attack mercury and its oxides. It decomposed at a temperature above 380°C .

During the current reporting period, samples of this film were analyzed using X-ray photoelectron spectroscopy (XPS) to determine the chemical state of this film. Only silicon, oxygen and a relatively small amount of mercury were detected by XPS, with chemical shifts corresponding to

elemental mercury and to silicon and oxygen as found in fused silica. This would indicate that the film was a mixture of elemental mercury and SiO_2 . However, the X-rays necessary for XPS are known to decompose mercury oxides by local surface heating.⁽²³⁾ Although no time dependence was observed for the chemical shift of the mercury XPS peak, it is still possible that the film had some other chemical structure which was rapidly decomposed by X-rays. A similar atomic composition was found on a region of the lamp surface where no film was visible. It is doubtful that the mercury in these clear portions was adsorbed directly from the mercury vapor in the lamp, since mercury is only weakly adsorbed onto silica.^(12,24) It is more likely that the film growth occurred to some extent over the entire lamp surface.

The tests described above indicate that the film is not composed solely of elemental mercury or of its oxides. It is doubtful that impurities play a major role in film growth, since impurity levels monitored during lamp filling were observed to be very low, and since no residual impurities were found in the film by EDAX and by XPS. As was mentioned in the previous interim report⁽¹²⁾, a possible chemical composition for the film is a mercury silicate. Although zinc and cadmium, which are directly above mercury in the periodic table, form silicates which have high melting points and are stable in most acids,⁽²⁵⁾ no detailed descriptions of a mercury silicate or of its preparation has been found in the literature.^(25,26,27,28) In fact, Röpke and Eysel⁽²⁸⁾ reported that they were unable to synthesize Hg_2SiO_4 from HgO and SiO_2 at elevated temperature and pressure. Therefore it is possible but unlikely that the film is composed of a mercury silicate. More likely compositions are a mixture of elemental mercury with SiO_2 and a mixture of mercury oxide with oxygen-deficient silica. The relative concentration of mercury, as determined by XPS, was small (about 3%), and it is plausible that this small amount of mercury or mercury oxide was protected from acid attack by the silica host (except, of course, for HF). The decomposition temperature of the film was slightly lower than that of HgO ,⁽²⁵⁾ and one would expect

that elemental mercury would be driven from the film by evaporation at a much lower temperature if the film were composed of elemental mercury and SiO_2 . Therefore, the most likely composition for the film is a mixture of mercury oxide and oxygen-deficient silica.

A possible growth mechanism for the film is a vapor-phase reaction between the mercury (ground-state or excited atoms, ions, or molecules) and the silicon and oxygen atoms sputtered from the silica surface by the plasma. Since mercury is only weakly adsorbed onto silica, and since no film growth has been observed in mercury cells which are exposed to resonant UV but not to a plasma discharge, the presence of the discharge is probably necessary for film growth. This hypothesis is consistent with the fact that the film accumulates mainly at the regions of weakest discharge, since any film grown in regions of strong discharge would be removed by the continuous sputtering. It is also consistent with the observation that the film appears to have been deposited from the vapor, as opposed to having grown by diffusion into the bulk.

The results of this investigation support the hypothesis that the interaction between mercury and fused silica is very weak, since the proposed chemical reactions only occur after the silica has been decomposed by sputtering. Other experimental techniques are being sought in order to characterize further the nature of this mercury-silica substance.

A presentation on this work was made at the March 1980 meeting of the American Physical Society, and a paper has been published in Applied Physics Letters. See Chapter 5 for further details on these publications.

5. PUBLICATIONS

5.1 THE DARK FILM IN MERCURY LAMPS

A presentation was made at the March, 1980 meeting of the American Physical Society in New York City [Paper # DI15, Bull.Amer.Phys.Soc. 25, 238 (1980) and a paper has been published in Applied Physics Letters 36, 963 (1980). The results are summarized in Section 4.5 of this interim report.

5.2 EFFECTS DUE TO QUADRUPOLE PERTURBATIONS

The work which is summarized in Chapter 2 of this interim report is described in greater detail in two Singer Company, Kearfott Division Technical Reports (references 11 and 14). Manuscripts are currently under preparation for submission to the Physical Review A. Tentative titles are "Quadrupole Perturbation Effects upon the ^{201}Hg Magnetic Resonance. I. Effects upon Free Precession of the Nuclear Spins," and "II. Relaxation due to an Anisotropic Perturbation."

5.3 USE OF NMR RELAXATION AS A SURFACE ANALYSIS TECHNIQUE

An abstract was submitted for presentation at the Fortieth Annual Conference on Physical Electronics, Ithaca, N.Y., June 1980. Unfortunately, it was not possible to include this paper in the conference schedule. The abstract appears below:

ADSORPTION OF MERCURY ON FUSED SILICA
OBSERVED USING OPTICALLY-PUMPED NUCLEAR MAGNETIC RESONANCE

P.A. Heimann and J.H. Simpson

Singer Co., Kearfott Div., Little Falls, N.J.

The relaxation of a distribution of oriented vapor-atom nuclear spins can serve as a sensitive probe of very weak interactions between such atoms and a solid surface. In experiments with mercury vapor and fused silica, we have used this technique to monitor heat-induced changes in the silica surface which have

not been observable using other techniques. We have also observed effects arising from the presence of a non-zero average electric field gradient at the mercury nucleus during physisorption. The technique is sensitive to surface-vapor interactions at temperatures where sticking times are on the order of 10^{-6} seconds or less, and it can detect changes as small as 10^{-18} eV in the average splitting between magnetic energy levels of the nucleus of the physisorbed atom.

We will describe the principles of optical pumping and relaxation of nuclear spins, and we will show how information on the strength and symmetry properties of the surface-vapor potential can be determined from measurements of relaxation rates. We use two stable isotopes of mercury: ^{199}Hg , which has a magnetic dipole moment and is affected by local magnetic fields, and ^{201}Hg , which in addition has an electric quadrupole moment and therefore is affected by both magnetic and electric fields. These local fields may arise, for example, from charged defects in the silica or from distortions in the mercury atomic charge distribution when the atom adsorbs onto the silica surface.

We will present results which indicate that the average strength of this interaction can vary by a factor of 10 or more between room temperature and 400°C , and can be altered more drastically by heating the silica to 900°C or by exposing the mercury to resonant uv light. Subsequent ESCA analysis of these samples showed no significant differences between those with strong and weak average surface fields. We will also present results which indicate that the electric field gradients, felt by the nucleus of the adsorbed atom as it hops about the surface, average to some non-zero value, directed normal to the surface. Several models for the origin of this average field gradient will be presented.

6. SUGGESTIONS FOR FURTHER STUDY

The results of investigations of relaxation due to a randomly-fluctuating quadrupole perturbation show that the torque and 2ω terms must be included along with the energy-shift term in order to describe the effects accurately. At present, the calculations of the effects of a steady-state quadrupole perturbation do not include these additional terms. Although their predictions are in agreement with experimental results, the calculations should be repeated, using all three terms of the quadrupole perturbation. New effects might be predicted by such a calculation.

Surface analysis of cell wall materials has determined that any impurities present are at concentrations less than one percent. More sensitive surface analysis techniques, such as secondary-ion mass spectroscopy, will be able to detect such impurities at lower concentrations. The surfaces of pyrex cells should also be analyzed, in order to help explain the long ^{199}Hg and short ^{201}Hg relaxation times observed in those cells. Other tests for the effects of impurities include experiments which will introduce certain impurities into the cell by diffusion through the cell wall and experiments which will attempt to remove charged impurities by means of a strong electric field applied at high temperatures (ion sweeping).

One unexplained property of the NMR cells is that they require a heat treatment after sealoff, despite the fact that they are heat treated before sealoff by baking on the vacuum system. It is now believed that the new surface created at the tip area during cell sealoff is not the major site for relaxation prior to the first post-sealoff heat treatment. Two hypotheses must still be considered:

1. The presence of mercury vapor during heat treatment is necessary for the beneficial effects of such a treatment. Therefore, the bakeout on the vacuum system is not sufficient to produce cells with long relaxation times.

2. The sealoff process causes some species to be released from the sealoff area and to be deposited over the entire cell surface. A post-sealoff heat treatment is required to eliminate the relaxing effects of this deposited species.

The first hypothesis can be tested by making "wet" cells, which have a droplet of liquid mercury in a reservoir attached to the cell. By controlling the temperature of the reservoir during heat treatment, the effects of heat treatment under vacuum and in the presence of mercury can be examined.

The species which is released from the sealoff area during sealoff could be a volatile impurity, such as alkali atoms, although these impurities are not present in large concentrations. Although silica glassblower's smoke might also be generated, it is not believed to be a strong relaxing site. However, the mechanism which was proposed for the dark film growth in mercury lamps might be occurring on a smaller scale during the cell sealoff: the silicon and oxygen which evaporates due to the intense heat at the sealoff tip reacts with the mercury vapor present in the cell to form a thin layer of the dark film material. Higher-sensitivity surface analysis might detect the presence of such a thin film, especially in cells whose sealoff tips were heated for a long period during sealoff. Experiments such as electron spin resonance might detect the presence of paramagnetic sites which could cause nuclear spin relaxation.

7. REFERENCES

1. D.S. Bayley, I.A. Greenwood, and J.H. Simpson, Final Report on Contract No. F44620-72-C-0047, August 1976, KD-76-31.
2. B. Cagnac and J. Brossel, C.R. Acad. Sc. Paris 249, 77 (1959).
3. W. Happer, "The Use of the Poincare Sphere to Analyze Faraday Readout Signals," Informal notes, KD-78-26 (unpublished).
4. G.H. Fuller and V.W. Cohen, Nucl. Data A5, 6 (1968), as cited in chapter 8b of American Institute of Physics Handbook, 3rd ed., D.E. Gray, ed., (McGraw-Hill, Inc., New York, 1977).
5. J.H. Simpson, Bull. Am. Phys. Soc. 23, 394 (1978).
6. C. Cohen-Tannoudji, Ann. Phys. (Paris) 7, 423 (1962) and 7, 469 (1962).
7. U. Fano, Rev. Mod. Phys. 29, 74 (1957). See also M.E. Rose, Elementary Theory of Angular Momentum (John Wiley & Sons, Inc., New York, 1957).
8. W. Happer, Phys. Rev. B1, 2203 (1970).
9. M. Rotenberg, R. Bivins, N. Metropolis and J.K. Wooten, Jr., The 3-j and 6-j Symbols (M.I.T. Press, Cambridge, Mass. 1959).
10. C.H. Volk, J.G. Mark, B.C. Grover, Phys. Rev. A20, 234 (1979).
11. P.A. Heimann, "Free Precession of a Spin-3/2 Atom in the Presence of a Quadrupole Perturbation," Technical Report KD-80-6 (unpublished).
12. P.A. Heimann, J.H. Simpson, and M.J. Kelly, Interim Progress Report on Contract No. F49620-76-C-0009, August 1979, KD-79-31.
13. W. Happer, Rev. Mod. Phys. 44, 169 (1972). See Table II, p.197 for a list of work on various relaxation mechanisms.
14. P.A. Heimann, "NMR Relaxation Due to an Anisotropic Perturbation," Technical Report KD-80-6 (unpublished).
15. Reference 13, p.200.
16. C.Cohen-Tannoudji, J. Physique 24, 653 (1963).
17. C.P. Slichter, Principles of Magnetic Resonance (Harper & Row, New York, 1963), p.172.

THE SINGER COMPANY • KEARFOTT DIVISION

18. Reference 13, p.201.
19. J.H. Simpson, V. Benischek, and D.S. Bayley, Interim Progress Report on Contract No. F49620-76-C-0009, October 1977, KD-77-49.
20. E.L. Hahn, Phys. Rev. 77, 297 (1950).
21. B. Cagnac (private communication). See also B. Cagnac and G.Lemeignan, C.R. Acad Sc. Paris 264, 1850 (1967).
22. J.H. DeBoer, The Dynamical Character of Adsorption (Oxford Univ. Press, New York, 1963).
23. L. Davis (private communication).
24. R. Liebich and P. Fink, Z. Chemie 11, 34 (1971).
25. R.C. Weast, ed. Handbook of Chemistry and Physics, 59th ed., Chemical Rubber Co., Cleveland (1978-79).
26. J.C. Bailar, H.J. Emeleus, R. Nyholm, A.F. Trotman-Dickenson, Comprehensive Inorganic Chemistry, Pergamon, Oxford (1973).
27. GMELIN Handbook of Inorganic Chemistry, System No. 34, Vol. 84, p. 1355, GMELIN Inst., Frankfurt (1969).
28. H. Ropke and W. Eysel, N. Jb. Miner. Mh., H.1, 1 (1978).

APPENDIX: RESEARCH OBJECTIVES & PERSONNEL

DESCRIPTION AND OBJECTIVES

This is a basic research program for investigating the interactions that cause relaxation of an initially established nonthermal angular distribution of the nuclear spins of odd mercury isotopes. The primary long range goal of the investigation is to understand the phenomena of spin-relaxation interactions between mercury and the walls of cells made from fused silica, glass, or modifications thereof. A major requisite for achieving this primary goal is the directly related secondary goal of developing procedures for fabricating cells with stable and predictable relaxation times, mercury vapor densities, and NMR signals elvels.

PERSONNEL

The following people were involved in this research effort during the reporting period.

Dr. James H. Simpson	Principal Investigator
Ivan Greenwood	Research Manager, Physics
Dr. Peter Heimann	Scientist
Dr. Michael Kelly	Senior Scientist
Edward Kling	Laboratory Assistant
Ralph Patterson	Scientist
Donald Shernoff	Senior Scientist
Dr. Robert Novick	Consultant

This report was prepared by P.A. Heimann, who also performed the calculation of the effects of quadrupole perturbations. Mercury cells were prepared and filled by D. Shernoff and M.J. Kelly. Measurements of cell properties, along with complementary observations, were performed by P.A. Heimann, except for the data in Section 2.4, which were supplied by

D. Shernoff and D.S. Bayley. The work was carried out at the Research Center of The Singer Company, Kearfott Division, Little Falls, N.J., except for the surface analysis of cell wall materials, which was performed at Perkin-Elmer, Physical Electronics Division, Eden Prairie, Minn.

EN
DAT
FILM